

3D self-consistent N -body barred models of the Milky Way

I. Stellar dynamics

R. Fux

Geneva Observatory, Ch. des Maillettes 51, CH-1290 Sauverny, Switzerland

Received April 23; accepted June 20, 1997

Abstract. Many 3D N -body barred models of the Galaxy extending beyond the Solar circle are realised by self-consistent evolution of various bar unstable axisymmetric models. The COBE/DIRBE K -band map, corrected for extinction, is used to constrain the location of the observer in these models, assuming a constant mass-to-light ratio. The resulting view points in the best matching models suggest that the inclination angle of the Galactic bar relative to the Sun-Galactic centre line is $28^\circ \pm 7^\circ$.

Scaling the masses according to the observed radial velocity dispersion of M giants in Baade's Window, several models reproduce satisfactorily the kinematics of disc and halo stars in the Solar neighbourhood, as well as the disc local surface density and scale parameters. These models have a face-on bar axis ratio $b/a = 0.5 \pm 0.1$ and a bar pattern speed $\Omega_P = 50 \pm 5$ km/s/kpc, corresponding to a corotation radius of 4.3 ± 0.5 kpc. The HI terminal velocity constraints favour models with low disc mass fraction near the centre.

The large microlensing optical depths observed towards the Galactic bulge exclude models with a disc scale height $h_z \lesssim 250$ pc around $R = 4$ kpc, arguing for a constant thickness Galactic disc. The models also indicate that a spiral arm starting at the near end of the bar can contribute as much as 0.5×10^{-6} to the optical depth in Baade's Window. The mass-to- K luminosity ratio of the Galactic bulge is probably more than 0.7 (Solar units), and if the same ratio applies outside the bar region, then the Milky Way should have a maximum disc.

Key words: Galaxy: structure, kinematics and dynamics

1. Introduction

Recent results demonstrate that the Milky Way, as more than 2/3 of disc galaxies and as suspected early on by

Send offprint requests to: R. Fux

de Vaucouleurs (1964) from a comparison of gas kinematics towards the Galactic centre and in external galaxies, is a barred galaxy with the near side of the bar pointing in the first Galactic quadrant. Evidence comes from near-IR surface photometry, discrete source counts, gas and stellar kinematics and gravitational microlensing (see Kuijken 1996 and Gerhard 1996 for reviews). The most suggestive data certainly are the COBE/DIRBE near-IR maps of the Galactic bulge (Weiland et al. 1994; Dwek et al. 1995; Binney et al. 1996 for a non-parametric deprojection). Estimates of the angle between the major axis of the bar and the Sun-Galactic centre line range from 10° to 45° (e.g. Stanek et al. 1997).

Furthermore, the distribution of HII regions, young stellar clusters, HI gas, CO clouds and dust betray the existence of several Galactic spiral arms (Mihalas & Binney 1981; Vallée 1995 and reference therein), and external spiral galaxies of the same (Sbc) Hubble type as the Milky Way have arm-interarm surface mass density ratios of order 2 out to at least 3 disc scale lengths from the centre (Rix & Zaritsky 1995). Hence the detailed structure of our Galaxy clearly deviates from axisymmetry.

No self-consistent 3D dynamical barred model of the Galaxy including simultaneously stellar, gas and dark components and extending beyond the Sun's Galactocentric distance has been proposed yet. Existing stellar dynamical models are either axisymmetric (Kuijken & Dubinski 1995; Durand et al. 1996) and/or restricted to a single Galactic component (Zhao 1996 for the COBE-bar; Kent 1992 and Kuijken 1995 for an axisymmetric bulge model), and gas flow calculations always assume a rigid rotating bar potential (Mulder & Liem 1986; Wada 1994; Weiner & Sellwood 1996).

This paper presents the first step of a program aiming such a complete model. Many self-consistent pure stellar dynamical barred models of the Milky Way are built from N -body evolution of bar unstable axisymmetric models. This method, already applied to the Galaxy by Sellwood (1985; 1993), naturally takes into account the main dy-

namical processes acting in the evolution of real isolated galaxies, like those responsible for spontaneous bar formation and self-sustained spiral structures (e.g. Zhang 1996). The N -body method also proves convenient to cope with a dissipative gas component, as will be added to the models in the next step and described in a second paper.

The structure of this paper is as follow: in Sect. 2 we describe the distinct initial conditions of the various components considered in the simulations. In Sect. 3, we give some technical informations about the N -body integration and present the time evolution of the initial models. In Sect. 4 we determine for each evolved model the best location of the observer (the Sun) according to the COBE/DIRBE near-IR observations of the Galactic bulge. In Sect. 5 we fix the velocity scales of the models to match the observed stellar velocity dispersion in Baade's Window and discuss some of the resulting absolute model properties.

2. Initial conditions

Equilibrium or close to equilibrium axisymmetric phase space density functions (DF) have been obtained for disc galaxies either by applying the strong Jeans theorem which states that the DF is an explicit function of at most three isolating independent integrals of motion (Kuijken & Dubinski 1995; Durand et al. 1996), or by solving the hydrodynamical Jeans equations for the velocity moments under some arbitrary closure conditions and assuming a Gaussian velocity distribution (Hernquist 1993).

The first method has the advantage to provide exact solutions of the Boltzmann equation, but is in general (except for Stäckel potentials) limited by the lack of an analytical third integral: DFs depending only on the two classical integrals, i.e. the total energy and the angular momentum about the symmetry axis (z), always have $\sigma_{Rz}^2 = 0$, unsuitable for substantially anisotropic spheroidal components, and $\sigma_{zz}^2 = \sigma_{RR}^2$, which in the Solar neighbourhood is wrong for any evolved stellar population. Moreover, generating DFs with imposed mass densities requires the cumbersome inversion of the integral equation that relates these two quantities (Kuijken 1995 and references therein).

The second method allows for a larger variety of velocity ellipsoids, depending on the closure conditions, and is also more adapted for specified mass distributions. It was therefore retained here, with some modification regarding the shape of the velocity distribution.

The initial models are described in standard astronomical units, assuming that the Galactocentric distance of the Sun is $R_\odot = 8$ kpc. These units will serve as reference in the evolved models until Sect. 5.

2.1. Mass distribution

The initial mass density ρ in our simulations includes three axisymmetric components.

The first one is an oblate stellar nucleus-spheroid (NS) inspired from the model of Sellwood & Sanders (1988):

$$\rho_{\text{NS}}(s) = \frac{M_{\text{NS}}}{4\pi a^3 e I_\infty} \cdot \frac{(s/a)^p}{1 + (s/a)^{p-q}}, \quad (1)$$

where

$$s^2 \equiv R^2 + z^2/e^2, \quad (2)$$

$$I_\infty = \frac{\pi}{p-q} \csc \left[\frac{(p+3)\pi}{p-q} \right], \quad (3)$$

a is a knee radius, e the axis ratio and M_{NS} the integrated mass. Setting $p = -1.8$ and $q = -3.3$, this mass density behaves as $s^{-1.8}$ for $s \ll a$, in agreement with near-IR observations of the Galactic inner kpc (Becklin & Neugebauer 1968; Matsumoto et al. 1982) if a constant mass-to-light ratio is assumed, and as $s^{-3.3}$ for $s \gg a$, similar to the radial number density decrease of RR Lyrae stars (Preston et al. 1991) and of the globular clusters (Zinn 1985). This component is therefore well suited to represent the nuclear bulge and the stellar halo.

The second component is a double exponential stellar disc:

$$\rho_{\text{D}}(R, z) = \frac{M_{\text{D}}}{4\pi h_R^2 h_z} \cdot \exp \left[-\frac{R}{h_R} - \frac{|z|}{h_z} \right], \quad (4)$$

where h_R , h_z and M_{D} are resp. the scale length, the scale height and the integrated mass. This component stands here for the Galactic old disc.

Finally an oblate exponential dark halo (DH) with the same axis ratio e as the NS component is added to ensure a flat rotation curve at large radii:

$$\rho_{\text{DH}}(s) = \frac{M_{\text{DH}}}{8\pi b^3 e} \exp(-s/b), \quad (5)$$

where b is the scale length and M_{DH} the total dark mass.

2.2. Truncation and flattening

To minimise the number of particles outside the force grid and increase the particle statistics near the centre (at fixed number of particles), we softly truncate each component multiplying its mass density by:

$$f(s) = \tanh \left[\frac{s - R_c}{2\delta} \right], \quad (6)$$

where R_c is the truncation radius and δ the width over which f falls from 1 to 0. The densities thus vanish on the spheroidal surface $s = R_c$.

In all simulations we set $R_c = 38$ kpc, $\delta = 5$ kpc and $e = 0.5$. The choice of e is realistic at least for the NS component and has the technical advantage over more spherical models to limit the z -extension of the force grid.

2.3. Choice of mass density parameters

The first row in Table 1 lists the values of the parameters a , M_{NS} , h_R , h_z , M_{D} , b and M_{DH} that were adopted for the “central” simulation m00. The choice of a and M_{NS} resp. refer to the transition radius where the Galactic near-IR emissivity starts to deviate significantly from the inner power law, and to a mass-to-light ratio in the nucleus region of 0.75 Solar units in the K -band, corresponding to a compromise between the values of 0.5 derived by Binney et al. (1991) from gas dynamics and 1 in Kent’s (1992) dynamical bulge model. The disc scales h_R and h_z are based on recent determinations (Fux & Martinet 1994; Ruphy et al. 1996; Sackett 1997 for a review) and are also consistent with near-IR photometry (Kent et al. 1991).

The last three parameters M_{D} , b and M_{DH} were adjusted to reproduce the Galactic rotation curve beyond 3 kpc, as illustrated in Fig. 1, while holding the local surface mass density of the disc into a reasonable range. The inner peak of the observed rotation curve is an artifact due to non-circular gas motion in the bar region and therefore does not need to be reproduced in axisymmetric models. The outer rotation curve of the resulting initial m00 model is fairly flat inside 25 kpc and then starts to decrease because of the exponential decline of the DH density and the mass truncation.

At $R = R_{\odot}$, the disc and total disc+NS+DH surface densities are resp. $48 M_{\odot}/\text{pc}^2$ (integrated over all z) and $66 M_{\odot}/\text{pc}^2$ within $|z| < 700$ pc, and the disc, NS and DH volume densities resp. 0.095 , $1.3 \cdot 10^{-3}$ and $0.014 M_{\odot}/\text{pc}^3$, summing up to give $\rho_{\text{tot}}(R_{\odot}, 0) = 0.11 M_{\odot}/\text{pc}^3$. Our local spheroid volume density exceeds estimates from low metallicity and high velocity stars (Bahcall et al. 1983). Part of the excess could be attributed to a missing thick disc component in the model.

The initial conditions need not to mimic precisely the Milky Way because the bar instability expected during time evolution will drastically affect the phase-space distribution. Since we do not control a priori the issue of a simulation, many runs are required to appreciate the effect of the initial parameters on the final properties of the evolved models. For this reason we have realised, in addition to the simulation m00, ten further simulations where each of the parameters a , M_{NS} , h_R , h_z and M_{D} has been separately set to a lower and higher value than in m00. The adopted values and nomenclature for each simulation are listed in Table 1. The DH parameters were always kept at the same values.

2.4. Isotropic Gaussian velocity distribution

Preliminary simulations (Fux et al. 1996) with isotropic and Gaussian initial velocity distribution for each component were performed to check how self-consistent evolution would rearrange the phase space distribution of such simple initial conditions.

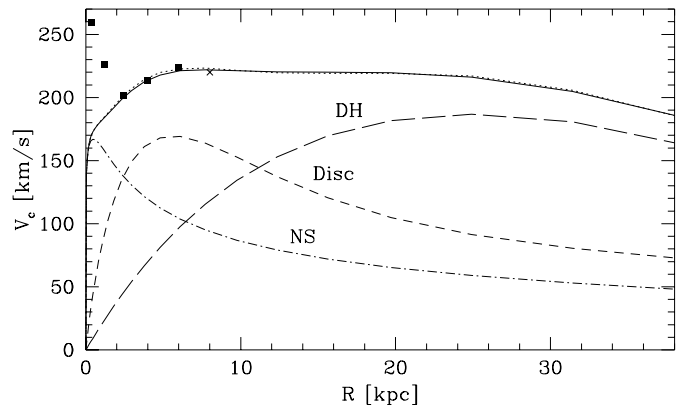


Fig. 1. Rotation curve of the initial m00 model, with the contributions of each component. The squares are tangent point circular velocities based on the HI terminal velocities compiled by Caldwell & Ostriker (1981), assuming $R_{\odot} = 8$ kpc and $V_{\odot} = 220$ km/s, as indicated by the cross. The almost coinciding full and dotted lines represent resp. the circular velocities before and after relaxing the DH component

Table 1. Mass density parameters of the initial models. Distances are in kpc and masses in $10^{10} M_{\odot}$. Model m00 is about centred in the explored parameter space. Unspecified values in the other models are similar to those in m00. Model m11 differ from m00 only by the DH kinematics and model m12 by the subsequent symmetry-free time integration. The parameters M_{NS} and M_{DH} are masses without the truncation by Eq. (6)

Model	a	M_{NS}	h_R	h_z	M_{D}	b	M_{DH}
m00	1.0	3.0	2.5	0.25	4.6	9.1	32.0
m01	2.0
m02	0.5
m03	.	1.6
m04	.	5.0
m05	.	.	2.0
m06	.	.	4.0
m07	.	.	.	0.13	.	.	.
m08	.	.	.	0.35	.	.	.
m09	4.2	.	.
m10	5.0	.	.
m11	.	.	non-rotating DH		.	.	.
m12	.	.	no symmetries		.	.	.

Simultaneous evolution of all mass components first led to unacceptable strong expanding rings of overdensity in the disc, mainly excited by radial mass oscillations of the DH damping out over a dynamical time scale. The DH was therefore individually relaxed during 3 Gyr with imposed axisymmetry before releasing the other components, suppressing indeed most of the subsequent perturbations in the disc. The origin of the DH disequilibrium will be discussed in Sect. 2.6.

In pre-relaxed DH simulations, the velocity dispersion of the disc becomes spontaneously anisotropic within a

few rotation periods, with a planar anisotropy compatible with first order epicycle theory (Binney & Tremaine 1987) and ratios between the velocity dispersion components around $R = R_o$ similar to those observed in the Solar neighbourhood for the old disc (see Fig. 2 in Fux et al. 1996 and Table 2). Hence isotropic initial kinematics seems to suffice for the disc.

However, the kinematics of the NS never reaches the observed radial velocity dispersion anisotropy of the local Galactic halo stars and instead sustains gravity through too fast rotation, exceeding half the circular velocity (see Fig. 3c and Table 2). The mean rotation velocity can of course be arbitrarily reduced by changing the sign of the azimuthal velocities of selected particles, but then the rotation velocity dispersion would increase and in turn deviate from the local observations. Some radial anisotropy should therefore appear already in the initial velocity distribution of the NS component.

2.5. Anisotropic velocity dispersion

To achieve higher degree of radial velocity dispersion anisotropy in both the NS and the DH components, we have solved the Jeans equations for more general closure conditions than just isotropy.

Following Bacon et al. (1983), we assume that the velocity ellipsoid points everywhere towards the Galactic centre, i.e. $\sigma_{r\theta}^2 = 0$ in spherical coordinates, with a free anisotropy parameter $\beta \equiv 1 - \sigma_{\theta\theta}^2/\sigma_{rr}^2$ depending only on r and of the form:

$$\beta(r) = \beta_\infty \frac{r}{\sqrt{r^2 + r_o^2}}, \quad (7)$$

where r_o is a transition radius and β_∞ the asymptotic anisotropy at large r : $\beta \propto r$ for $r \ll r_o$, and $\beta = \beta_\infty$ for $r \gg r_o$. We also assume no other streaming motion than rotation about the symmetry axis, i.e. $\overline{v_r} = \overline{v_\theta} = 0$, and take as boundary conditions $\sigma_{rr}^2 = \sigma_{\theta\theta}^2 = 0$ on the mass truncation surface. The details of the numerical method, which can in fact also handle anisotropy parameter depending on θ , are presented in Fux (1997).

The solutions provide $\overline{v_\phi^2} = \overline{v_r^2} + \sigma_{\phi\phi}^2$, leaving free the relative contributions of organised and random velocity in the ϕ direction. As a convenient choice, which ensures isotropy near the centre and low rotation for $r \gg r_o$, we set:

$$\sigma_{\phi\phi}^2 = \frac{r_o^2 \sigma_{\theta\theta}^2 + r^2 \overline{v_\phi^2}}{r_o^2 + r^2}, \quad (8)$$

where r_o is the same parameter as in Eq. (7).

The values of r_o and β_∞ are restricted by the condition $\overline{v_\phi^2} \geq 0$ everywhere. In particular, on the truncation surface of our initial mass models, this condition imposes an upper limit to $\beta(r)$ in the range $eR_c < r < R_c$ depending only on the potential and its first derivatives (see Fig. 2). The resulting strongest constraint is $\beta(eR_c) < 0.65$.

Table 2. Observed properties of the stellar halo (subdwarfs) and the old disc in the Solar neighbourhood. Σ_o is the *total* thin disc surface density (i.e. including also the young disc). The values of the disc velocity dispersion are averages over z . References are: (1) Majewski 1993, (2) Wielen 1977, (3) Sackett 1997, (4) Kuijken & Gilmore 1989

			Reference
Subdwarfs:	$\sigma_{rr} = \sigma_{RR}$	131 ± 6 km/s	1
	$\sigma_{\phi\phi}$	106 ± 6 km/s	1
	$\sigma_{\theta\theta} = \sigma_{zz}$	85 ± 4 km/s	1
	$\overline{v_\phi}$	37 ± 10 km/s	1
Old disc:	σ_{RR}	48 ± 3 km/s	2
	$\sigma_{\phi\phi}$	29 ± 2 km/s	2
	σ_{zz}	25 ± 2 km/s	2
	h_z	300 ± 25 pc	3
Thin disc:	Σ_o	$48 \pm 8 M_\odot/\text{pc}^2$	4

2.6. Dark halo disequilibrium and velocity distribution

Coming back to the DH radial oscillations, single relaxation of DHs with Gaussian initial velocity distributions but variable radial velocity dispersion anisotropy based on the technique outlined above (Sect. 2.5) indicate that the oscillations strengthen with the amount of anisotropy. From these experiments we inferred that the mass oscillations are in fact a consequence of the Gaussian tails in the velocity distribution and the finite DH mass extent: a significant fraction of the DH particles, about 10% in the isotropic case and increasing with radial anisotropy, have velocities which carry them outside the truncation surface, unbalancing therefore the inner equilibrium.

To overcome this problem, the Gaussian velocity distributions of the extended DH *and* NS components have been replaced by a bounded 3D distribution build upon standard Beta distributions. This new “ B_3 ”-distribution has four parameters, κ , λ , μ and ω (one per adjustable velocity moment), and is described as a function of its reduced variables ξ , η and ζ in Appendix A.

With the substitutions $\xi \equiv v_\phi/v_o$, $\eta \equiv v_r/v_e$ and $\zeta \equiv v_\theta/v_e$, the distribution is bounded in velocity space by a spheroidal surface with principal axes aligned with the v_ϕ , v_r and v_θ axes and of half-length v_o along v_ϕ and v_e along v_r and v_θ . The boundary surface is not taken as a sphere because particles launched at a given spatial position can afford higher velocities in the tangential direction than in the radial direction without escaping the system. Indeed, the boundary velocities v_o and v_e can be quantified using the integrals of motion. If the velocity of a particle is decomposed in an azimuthal component, v_ϕ , and a meridional component, v_m , then its energy writes $E = \frac{1}{2}(v_m^2 + L_z^2/R^2) + \Phi$, where $L_z = R \cdot v_\phi$ is the angular momentum about the z -axis and $\Phi(R, z)$ is the gravitational potential. Assuming that the mass density is bounded by an equipotential surface Φ_p and imposing $v_m = 0$ when a particle reaches this surface (otherwise the

particle would cross the surface and escape), the conservation of energy and angular momentum yield the following condition for the confinement of the particle orbit inside the system:

$$v_{\text{in}}^2 + \frac{R_{\text{p}}^2 - R^2}{R_{\text{p}}^2} v_{\phi}^2 < 2[\Phi_{\text{p}} - \Phi(R, z)], \quad (9)$$

where R_{p} is the maximum cylindrical radius attained by the particle. Thus:

$$v_{\text{e}} = \sqrt{2(\Phi_{\text{p}} - \Phi)}, \quad (10)$$

$$v_{\text{o}} = \frac{R_{\text{p}}}{\sqrt{R_{\text{p}}^2 - R^2}} \cdot v_{\text{e}}, \quad (11)$$

and $v_{\text{o}} > v_{\text{e}}$.

In our initial models, since the truncation surface of the mass distribution is not an equipotential, we simply take the maximum value of the potential on this surface, i.e. $\Phi_{\text{p}} \equiv \Phi(R_{\text{c}}, 0)$, and set $R_{\text{p}} = R_{\text{c}}$. For the initial m00 model, the resulting behaviour of v_{e} and v_{o} in the plane is shown in Fig. 3a. This will not prevent some particles to escape but at least considerably reduces the DH disequilibrium and ensures well defined values of the boundary velocities everywhere inside the truncation surface.

If $\kappa, \lambda \leq 2$, $\mu \leq 3/2$ or $\omega \leq 1$, the velocity distribution presents unphysical singularities on the boundary spheroid which should in principle be avoided. In particular, assuming $\overline{v_{\phi}} > 0$ and substituting the requirement $\lambda > 2$ in Eq. (A10) yields:

$$\overline{v_{\phi}} > \frac{-(v_{\text{o}}^2 - \overline{v_{\phi}^2}) + \sqrt{(v_{\text{o}}^2 - \overline{v_{\phi}^2})^2 - 16v_{\text{o}}^2(v_{\text{o}}^2 - 5\overline{v_{\phi}^2})}}{8v_{\text{o}}}, \quad (12)$$

which puts a lower limit on the mean rotation velocity, and thus further restricts the range of the parameter r_{o} . For the adopted mass truncation radius R_{c} and flattening e , this condition unfortunately prevents NS models with mean rotation velocity below 100 km/s when approaching $R = R_{\text{c}}$ (see Fig. 3a). Therefore, to reproduce the observed rotation of the stellar halo in the Solar neighbourhood with Eq. (8), we decided to violate this condition for the NS component and accept irregular velocity distributions in a minor portion of the $R-z$ plane. Similarly, the requirements $\mu > 3/2$ and $\omega > 1$ put constraints on the meridional components of the velocity dispersion which could be satisfied in all NS models, but not in the hot central part of the DHs.

The DH pre-relaxations have been maintained even with the adopted B_3 velocity distribution to minimise any persistent DH induced perturbations on the visible components. For these components, the Jeans equations were solved using the total potential *after* relaxation, the noise in the potential being reduced by averaging the DH mass density in time. The DH relaxation does not modify much the starting potential (see Fig. 1).

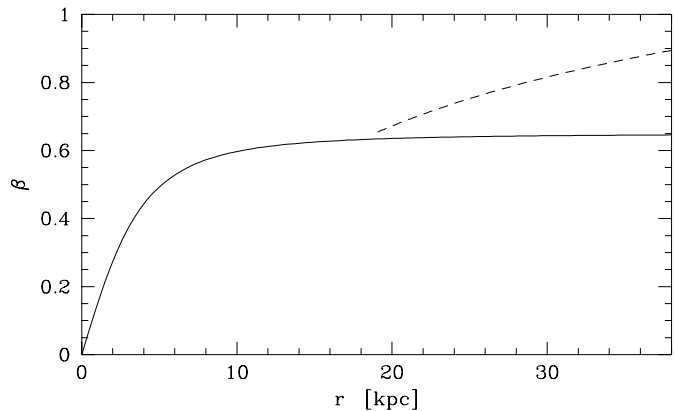


Fig. 2. Full line: anisotropy parameter $\beta(r)$ of the NS component in all initial models. Dashed line: upper limit for positive $\overline{v_{\phi}^2}$ on the mass truncation surface (in model m00)

2.7. Choice of velocity parameters

For the NS of simulation m00, the parameters r_{o} and β_{∞} were adjusted to reproduce the observed rotation and velocity dispersion of the stellar halo in the Solar neighbourhood given in Table 2. The adopted parameters are $r_{\text{o}} = 4.3$ kpc and $\beta_{\infty} = 0.65$, leading to the very close to critical $\beta(r)$ profile displayed in Fig. 2. The resulting initial velocity moments of the NS are shown in Fig. 3a.

The reversal of the σ_{rr}^2 versus $\sigma_{\phi\phi}^2$ anisotropy at $R \approx 13$ kpc is consistent with the kinematics of the blue horizontal branch field stars (Sommer-Larsen et al. 1994) and other halo stars (Beers & Sommer-Larsen 1995). The azimuthal anisotropy at large radii could reflect the fact that stars easier escape in the radial direction, and that σ_{rr}^2 must vanish on the boundary of a finite and stationary system, whereas $\sigma_{\phi\phi}^2$ can still be supported by low eccentricity orbits.

Figure 3b shows the NS kinematics in simulation m00 shortly before the formation of the bar. Within $R \lesssim 14$ kpc, the NS loses a part of its radial velocity dispersion anisotropy and its rotation velocity raises. These changes certainly reflect the extreme nature of our initial conditions, i.e. forcing the radial anisotropy to its maximum. Nevertheless, the re-adjusted velocity moments still remain much closer to the observations than those of simulations started with isotropic NS velocity dispersion, as illustrated in Fig. 3c.

For the NS of the other simulations, we simply use the same r_{o} and β_{∞} values than in simulation m00. For the DHs of simulations m00-m10, we set $r_{\text{o}} = b$ and $\beta_{\infty} = 0.1$, compatible with the restriction of Eq. (12). The initial conditions for simulation m11 are identical with those of m00, except that the DH has the same anisotropy $\beta(r)$ as the NS and no net rotation, i.e. $\sigma_{\phi\phi}^2 = \overline{v_{\phi}^2}$ instead of Eq. (8), and hence also present an irregular outer v_{ϕ} -distribution. As justified by the preliminary simula-

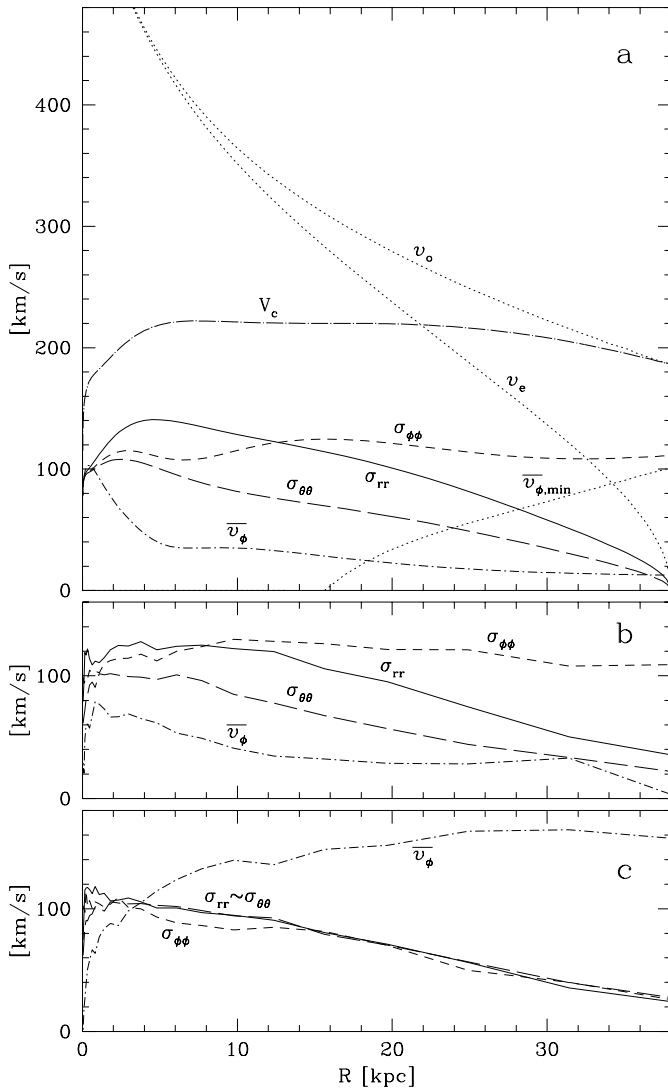


Fig. 3. **a** Initial velocity dispersion and mean rotation velocity of the NS component at $z = 0$ in simulation m00. The two upper dotted lines give the meridional (v_e) and azimuthal (v_o) escape velocities resulting from Eqs. (10) and (11), and the lower dotted line the minimum admissible mean rotation ($\overline{v}_{\phi,\min}$) defined in Eq. (12) for regular velocity distribution. The circular velocity (V_c) is also represented. **b** Corresponding velocity moments at $t = 1200$ Myr. **c** Velocity moments at the same time in a simulation identical to m00 except that the NS component has isotropic initial velocity dispersion

tions, all discs have isotropic ($\beta = 0$) and Gaussian initial velocity distribution, implying a velocity dispersion tightly related to their scale heights.

3. Time evolution

The simulations m00-m11 were all done imposing 2-fold rotational symmetry about the z -axis and reflection symmetry about the plane $z = 0$, hence reducing the numerical noise of the potential. For comparison, the initial

m00 model was also integrated without any symmetry, providing our last m12 simulation. Each simulation is run up to $t = 5$ Gyr, and outputs of the particle phase-space coordinates were realised every 200 Myr, leaving 325 evolved models to analyse.

The number of particles is fixed to 10^5 for the NS+disc components and 10^5 for the DH. The proportion of particles in the NS and in the disc is such that the particle masses are exactly the same for both components, and may therefore change from one simulation to another: e.g. 30262 NS particles and 69738 disc particles for m00.

3.1. N -body code

The initial models are integrated with the Particle-Mesh code described in Pfenniger & Friedli (1993).

The potential is computed on a cylindrical polar grid using the fast Fourier transform technique in the ϕ and z dimensions, where the cells are equally spaced. The radial spacing of the cells is logarithmic with a linear core to avoid an accumulation point at the centre. The short range forces are softened by a variable homogeneous ellipsoidal kernel with semi-axes set to 1.1 times the respective cell dimensions. The adopted grid has $25(R) \times 24(\phi) \times 201(z)$ cells and extends up to 50 kpc in R and ± 20 kpc in z , corresponding to a radial resolution of 40 pc at the centre and about 1.8 kpc at R_o .

The orbits are integrated using the standard leap-frog algorithm with a time step of 0.1 Myr, representing a fraction of the crossing time of the central grid mesh in the steep NS potential.

3.2. Model evolution

Figure 4 illustrates the evolution of our 13 simulations. They all lead to the formation of a bar, but not always on the same time scale. Models with higher initial values of Toomre's axisymmetric stability parameter Q in the region of rising circular velocity need more time to develop the bar, in agreement with the work of Athanassoula & Sellwood (1986). This is the case for example when comparing the simulations m07 and m08: the former starts with a much colder disc, i.e. a lower value of Q , and indeed forms the bar more quickly.

The size of the bars clearly varies from one simulation to the other. However, one must keep in mind here that the evolved models can always be separately rescaled to look more similar than they do in initial units, hence complicating an objective comparison. All bars finally flatten the surrounding radial profile of the disc, the effect being particularly marked in simulation m03.

Some simulations obviously pass through a double bar phase, like in m04t4400. The simulations also develop transient spiral arms, especially strong during the time of bar formation. Such structures would be hard to achieve by other means than the N -body technique.

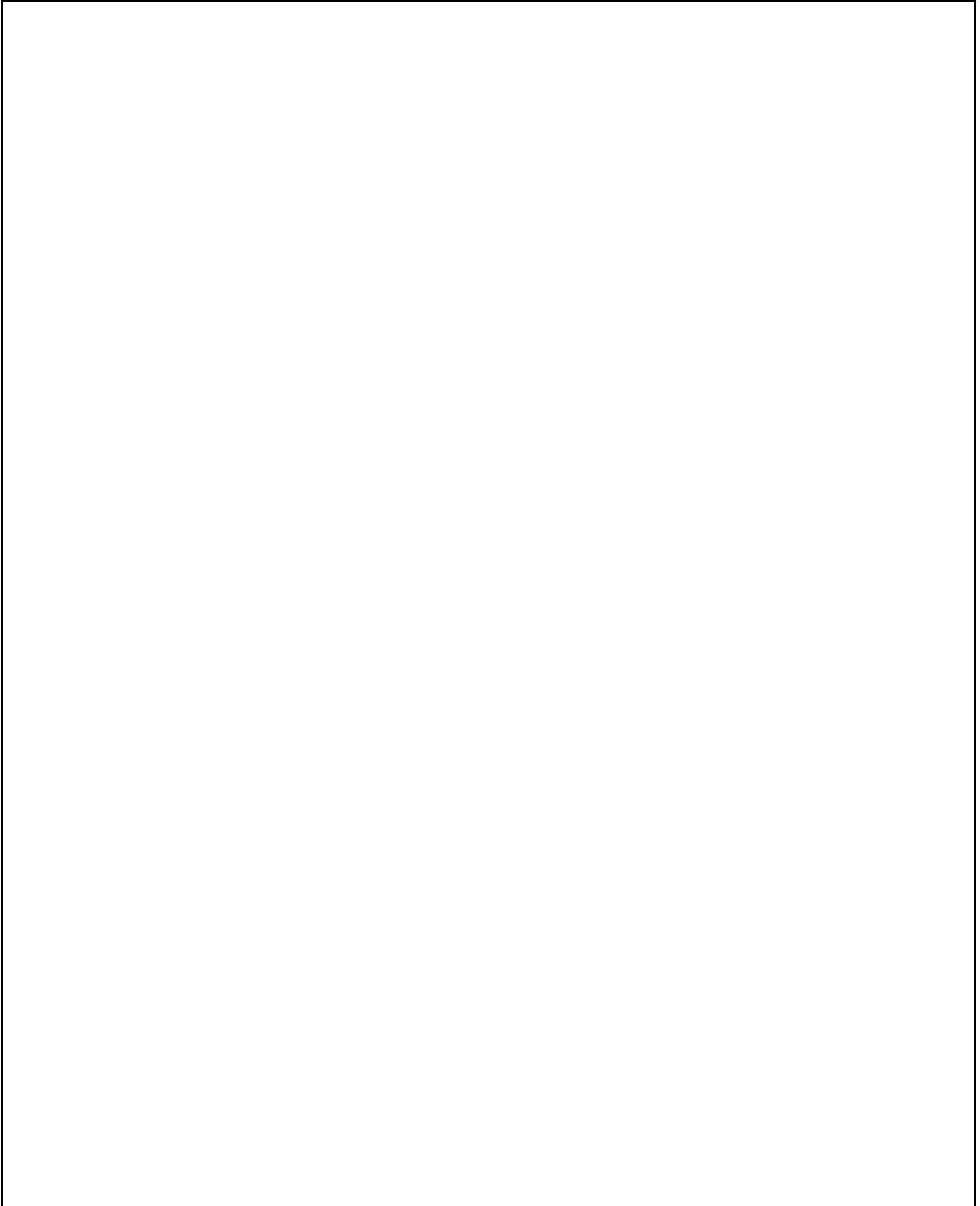


Fig. 4. Face-on surface density evolution in all runs, including 1/3 of all investigated models. The distances are in initial units and the contours are spaced with one magnitude interval. Rotation is clockwise. Note the induced asymmetries in run m12

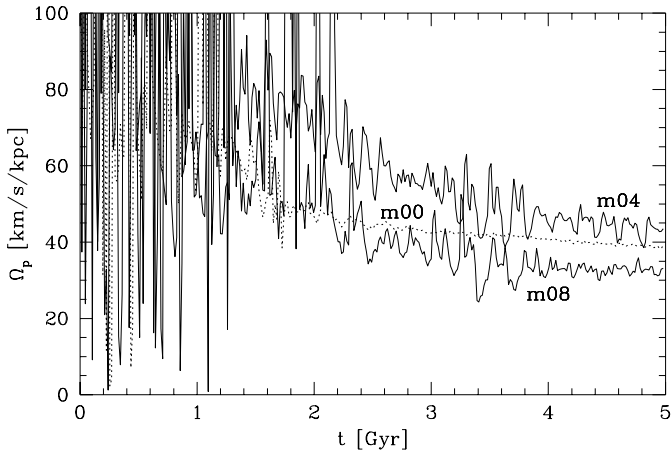


Fig. 5. Pattern speed $\Omega_P(t)$ of the bar in simulations m00, m04 and m08 (initial units). The pattern speed in the other simulations roughly fall within the gap delimited by the m04 and m08 solid lines

Figure 5 shows the bar pattern speed $\Omega_P \equiv \frac{d\vartheta}{dt}(t)$ as a function of time in three simulations. The azimuthal angle ϑ of the bar major axis (in the inertial frame) is calculated by diagonalising the I_{xx} , I_{yy} and I_{xy} components of the moment of inertia tensor of the NS+disc particles inside $R < R_e$, where R_e is the radius extremising the ratio of the inferred diagonal components. The noise level in the $\Omega_P(t)$ curves depends on the bar strength and on the presence of multiple rotating patterns.

After the first bar rotations, where the bar may slow down by up to 15 km/s/kpc/Gyr, $\Omega_P(t)$ is in general constant or slowly decreasing with a rate of a few km/s/kpc/Gyr. The lower rotation of the DH in simulation m11 does not influence the pattern speed of the bar: $\Omega_P(t)$ in m11 is almost the same as in m00. Simulation m12 has a faster $\Omega_P(t)$ decline than m00, probably related to its noisier gravitational potential.

The presence of a dissipative gas component may alter the bar evolution by speeding up its angular velocity and causing its dissolution (Friedli & Benz 1993).

4. Location of the observer

The Diffuse Infrared Background Experiment (DIRBE) onboard the COBE satellite has mapped the full sky in ten different bands, ranging from $1.25\mu\text{m}$ to $240\mu\text{m}$, with a resolution of $0^\circ.7 \times 0^\circ.7$ and a field spacing of approximately $0^\circ.32$. The maps at 1.25 (J -band), 2.2 (K -band), 3.5 and $4.9\mu\text{m}$, dominated by integrated stellar light, clearly show an asymmetric boxy/peanut shaped bulge betraying the underlying bar (Weiland et al. 1994).

The K -band map offers a good compromise between maximum stellar emissivity, low extinction by dust and small relative contribution of zodiacal light. If a constant mass-to-light ratio is assumed throughout the Galaxy, it

should therefore provide a reliable tracer of the integrated mass distribution and thus put severe constraints on dynamical models of the Milky Way.

This section presents a technique to find the view point in an N -body galaxy from where the simulated panorama most resembles a fixed map, and applies the method to our models and a deredened version of the COBE K -band data.

4.1. Reduction of the COBE K -band map

Even if extinction in the infrared is much less than in the optical, it is still not negligible (about 1.5 magnitude in K towards the Galactic centre).

Thus, following Arendt et al. (1994), the raw K -band map has been corrected for foreground dust extinction by first building a $J-K$ color excess map under the assumption of constant intrinsic color, taken as the average color in the region $l < 30^\circ$ and $10^\circ \leq b \leq 15^\circ$, and then transforming it into a K -band optical depth map using the reddening law of Rieke & Lebofsky (1985). Such a correction however is not valid for $|b| \lesssim 3^\circ$ where a significant fraction of the integrated light is emitted along the dust screen. Hence this low latitude region must be excluded in the fitting procedure.

Finally, the dust subtracted map has been symmetrised in b and converted from its COBE Quadrilateralised Spherical Cube representation to a cartesian grid map in Galactic coordinates with $\Delta l = \Delta b = 1^\circ$ pixel size, as shown in Fig. 6. This resolution ensures sufficient particle statistics per pixel when computing model maps without blurring too much the data.

4.2. Fitting method

The position of the observer in the models is specified by its distance \tilde{R} in initial units from the ‘‘Galactic’’ centre and the scale free-angle φ between the line joining himself to the centre and the major axis of the bar, with positive φ when the bar is leading the observer. We assume that the observer lies in the plane of symmetry, i.e. $z_o = 0$, and that the visible components have a constant mass-to-light ratio Υ_K in the K -band. Hence model maps of integrated light will depend on \tilde{R} , φ and Υ_K .

The flux per unit solid angle in a given pixel i is estimated from Monte Carlo integration:

$$F_i(\tilde{R}, \varphi, \Upsilon_K) = (\Upsilon_K \Delta\Omega)^{-1} \sum_{k=1}^{N_i} \frac{m}{D_k^2 + \varepsilon^2}, \quad (13)$$

where the sum ranges over all NS+disc particles inside pixel i , N_i is the total number of such particles, m the mass per particle (identical for both visible components), D_k the distance of the k^{th} particle relative to the observer, ε a softening parameter to reduce the statistical noise induced by the closest particles ($\varepsilon^2 = 0.1$), and $\Delta\Omega$ the solid

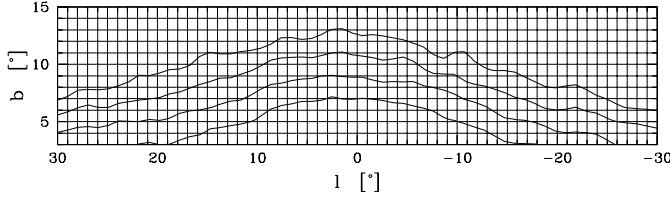


Fig. 6. Grid used for the data interpolation and the model flux calculation in the COBE-map fitting. The solid lines roughly delimit the 100, 200, 300 and 400 pixels which in the models have the best particle statistics

angle sustained by the pixel. If b_1 and $b_2 = b_1 + \Delta b$ are the pixel limits in Galactic latitude, then:

$$\Delta\Omega = \Delta l(\sin b_2 - \sin b_1). \quad (14)$$

The three parameters \tilde{R} , φ and Υ_K are adjusted to the COBE/DIRBE K -band data by minimising the mean quadratic relative residual between model and observed fluxes *corrected* for statistical noise, i.e. (see Appendix B):

$$\mathcal{R}^2(\tilde{R}, \varphi, \Upsilon_K) = (\chi^2 - \nu) \left[\sum_{i=1}^{N_{\text{pix}}} \frac{F_i'^2}{\sigma_i'^2} \right]^{-1}, \quad (15)$$

where

$$\chi^2 = \sum_{i=1}^{N_{\text{pix}}} \frac{(F_i - F_i^\circ)^2}{\sigma_i^2}, \quad (16)$$

N_{pix} is the number of pixel, $\nu = N_{\text{pix}} - 3$ the number of degree of freedom, F_i° the observed flux in pixel i , and σ_i^2 the variance of F_i , whose best estimate reduces to (see Appendix C):

$$\sigma_i^2 = (\Upsilon_K \Delta\Omega)^{-2} \sum_{k=1}^{N_i} \left(\frac{m}{D_k^2 + \varepsilon^2} \right)^2. \quad (17)$$

The data supply much more accurate fluxes than the models, so that their errors may be neglected.

The standard χ^2 minimisation method was abandoned because the χ^2 strongly depends on the precision of the F_i 's. In particular, the χ^2 value will systematically increase with the number of particles available to compute the model maps (except for perfect models). Thus the fitted view points are biased towards regions where the model maps are noisier, and the relative quality of different models cannot be judged from this indicator alone. Furthermore, the fact that the σ_i^2 's are only approximations of the true variances causes an overestimation of the χ^2 increasing with the uncertainties on the variances, which biases the solutions in the opposite way. This bias persists even in \mathcal{R}^2 adjustments since \mathcal{R}^2 depends explicitly on χ^2 . To reduce its effect, the σ_i^2 's have been averaged over the neighbouring pixels.

Only the bulge region $|l| < 30^\circ$ and $3^\circ < b < 15^\circ$ enclosing the bar and with reliable dust correction, representing 720 pixels, is included in the fits. Moreover, to exclude pixels with low number of particles and to check the consistency of the fitted parameters with respect to the selected $l-b$ sub-region, the pixels are sorted by decreasing N_i and only the most populated are retained, with N_{pix} between 100 and 400. The typical $l-b$ regions selected this way are indicated in Fig. 6.

For each model, \mathcal{R}^2 is computed on a 2D grid in \tilde{R} and φ with resolution $\Delta\tilde{R} = 0.1$ kpc and $\Delta\varphi = 1^\circ$. The parameter Υ_K does not require an extra dimension, since for fixed values of \tilde{R} and φ the optimum Υ_K , which minimises \mathcal{R}^2 , can be calculated analytically as:

$$\Upsilon_{K,\min}(\tilde{R}, \varphi) = \left(\sum_{i=1}^{N_{\text{pix}}} \frac{F_i'^2}{\sigma_i'^2} - \nu \right) \left(\sum_{i=1}^{N_{\text{pix}}} \frac{F_i' F_i^\circ}{\sigma_i'^2} \right)^{-1}, \quad (18)$$

where the primes indicate that the Υ_K factor in Eqs. (13) and (17) is removed. The \mathcal{R}^2 -grid is then smoothed by averaging \mathcal{R}^2 over the 3×3 nearest grid points and the resulting minimum defines our best fit position of the observer.

4.3. Tests

The method has been tested with a simple mass model consisting in a triaxial multi-normal bulge for the bar and an axisymmetric Miyamoto-Nagai (1975) disc:

$$\rho_{\text{test}}(x, y, z) = \frac{M_1}{\sqrt{8\pi^3} \sigma_x \sigma_y \sigma_z} \exp \left[-\frac{1}{2} \left(\frac{x^2}{\sigma_x^2} + \frac{y^2}{\sigma_y^2} + \frac{z^2}{\sigma_z^2} \right) \right] + \frac{b_M^2 M_2}{4\pi} \left[\frac{a_M R^2 + (a_M + 3z_b)(a_M + z_b)^2}{(R^2 + (a_M + z_b)^2)^{5/2} z_b^3} \right], \quad (19)$$

where $R^2 = x^2 + y^2$, $z_b^2 = z^2 + b_M^2$, and with $\sigma_x = 1.5$, $\sigma_y = 0.8$, $\sigma_z = 0.4$, $a_M = 5$ and $b_M = 0.3$. The Miyamoto-Nagai component is truncated at $R = 15$ and its mass within this radius is $3M_1$.

COBE-like maps were computed for several *input* observing points $(R_{\text{in}}, \varphi_{\text{in}})$ in the test model and 100 distinct discrete realisations of this model with 10^5 particles, as in the NS+disc components of the dynamical models, were fitted to these maps by \mathcal{R}^2 minimisation, yielding the *output* observing points $(R_{\text{out}}, \varphi_{\text{out}})$. The statistics of the results is shown in Fig. 7.

For $\varphi_{\text{in}} \lesssim 40^\circ$ and $R_{\text{in}} \lesssim 10$, the systematic and statistical errors on φ_{out} are at most $+2^\circ$ and 5° (except at small R_{in} for $N_{\text{pix}} = 100$). For $N_{\text{pix}} \geq 200$, the statistical error on R_{out} is less than 4%, and R_{out} is underestimated with a systematic error increasing with N_{pix} , which is intimately connected with the χ^2 bias already mentioned in Sect. 4.2: the additional pixels in the low flux region have the most uncertain σ_i^2 's and thus artificially enhance the value of \mathcal{R}^2 , as indicated in the top plots of Fig. 7.

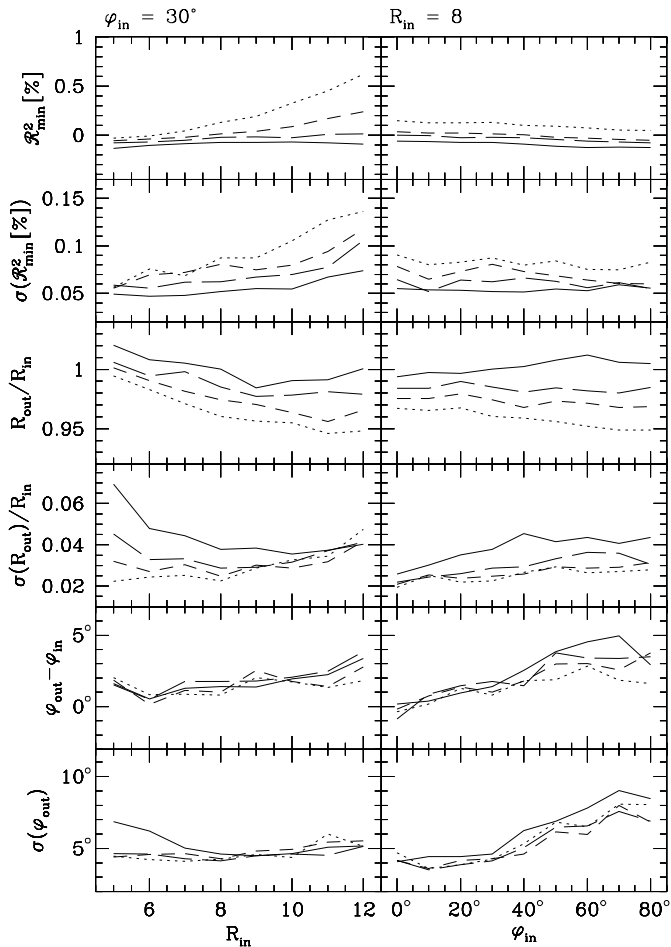


Fig. 7. Test results of the \mathcal{R}^2 minimisation technique. R_{in} and φ_{in} are the correct input coordinates of the observer and R_{out} and φ_{out} the corresponding adjusted output parameters. The left and right columns are resp. for variable R_{in} and fixed φ_{in} , and for fixed R_{in} and variable φ_{in} . From top to bottom, based on 100 experiments for each input position: the averages and standard deviations of \mathcal{R}^2 at the minimum, R_{out}/R_{in} and φ_{out} . The full, long-dashed, short-dashed and dotted lines stand resp. for $N_{pix} = 100, 200, 300$ and 400

4.4. Application

The \mathcal{R}^2 method has been applied to all dynamical models, noting φ_o and \tilde{R}_o the best fit parameters of the observer and \mathcal{R}^2_{min} the value of \mathcal{R}^2 at the minimum. An example of \mathcal{R}^2 topography is given in Fig. 8.

As a compromise between maximum exploitation of the data and minimum systematic errors on the fitted view point parameters, we have privileged the case $N_{pix} = 300$ and sorted the models by increasing $\mathcal{R}^2_{min}(300)$. This model sequence was then truncated to include at least two models of each simulation, resulting in a sample of 68 models with $\mathcal{R}^2_{min}(300) \leq 0.756\%$ (hereafter our “A” sample).

Figure 9 shows the distribution of the adjusted angles φ_o for the models belonging to this sample as a function of

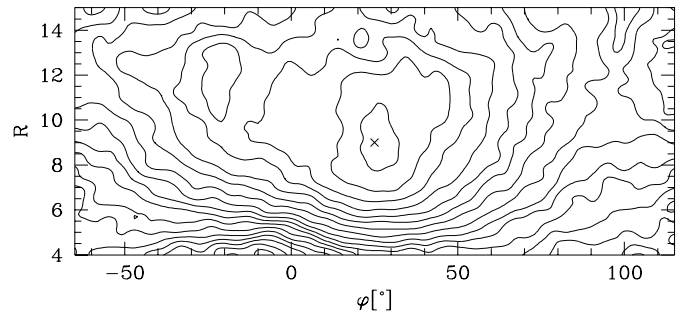


Fig. 8. \mathcal{R}^2 solution for the location of the observer in model m08t3200, for $N_{pix} = 300$. The \mathcal{R}^2 contours are spaced by 0.5% and the cross indicates the position of the minimum. The parameter Υ_K has been substituted using Eq. (18)

N_{pix} . Taking into account the uncertainties of the individual angles, due to the moment of inertia method for determining the absolute angular position of the bar major axis and to the intrinsic standard deviation of the \mathcal{R}^2 method, the 40 best models support an angle of $\varphi_o = 28^\circ \pm 7^\circ$ for the Galactic bar, with a possible overestimation by 2° according to the tests.

This result is consistent with the value of $20^\circ - 30^\circ$ found recently by the OGLE team from the color magnitude diagram of red clump giants in several fields across the Galactic bulge (Stanek et al. 1997) and with the upper limit of 30° set by the MACHO microlensing constraints (Gyuk 1996), and confirms the privileged 25° obtained by the deprojection of the properly dust subtracted L -band COBE map (Binney et al. 1996; Bissantz et al. 1996).

The best models regarding the COBE constraints come from simulation m08, started with the thickest and hottest disc. Indeed five of the six lowest residual models are from this simulation, with $\mathcal{R}^2_{min}(300) \approx 0.3-0.4\%$. For comparison, the initial m00 model has $\mathcal{R}^2 \geq 2.4\%$ everywhere. Nevertheless, we note that model m06t4600 gives the best COBE-data match within the entire $|l| < 90^\circ$ region. This model has a low disc scale height, close to the 204 pc derived by Kent et al. (1991) from the Spacelab IR Telescope data with the assumption of constant h_z .

Table 3 lists the results for a selection of A sample models (hereafter our “B” sample) which, in addition to the COBE constraints, also best reproduce observations in the Solar neighbourhood (see Sect. 5.1). The simulation m00 provide no acceptable model to enter this sub-sample.

The distance scale S_R of the models now directly follows by setting the best-fit Galactocentric distance of the observer for $N_{pix} = 300$ to $R_o = 8$ kpc. Figure 10 presents the NS+disc face-on configurations of some B sample models after such rescaling and the confrontation of these models to the COBE data. The B sample models have a face-on surface density axis ratio $b/a = 0.5 \pm 0.1$ for the contours crossing the bar major axis at $R = 2-3$ kpc.

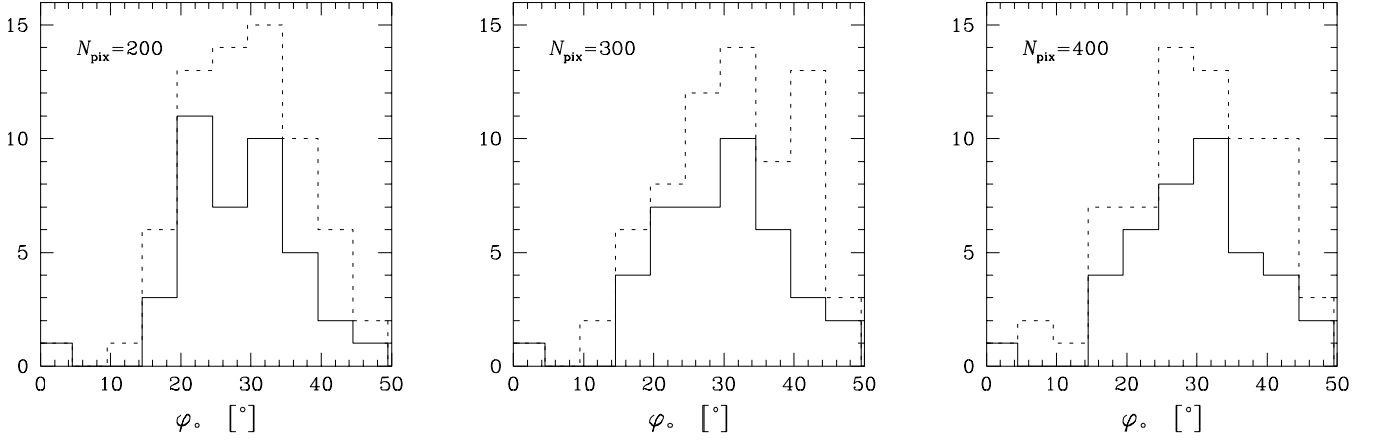


Fig. 9. Distribution of the best-fit position angle φ_0 of the bar in the dynamical models. Dashed line: including all 68 models of the A sample; full line: including only the 40 lowest \mathcal{R}_{\min}^2 models of this sample

Table 3. Location of the observer in the final selection of models (B sample), as constrained by the COBE/DIRBE dereddened K -band map. The models are sorted by increasing \mathcal{R}_{\min}^2 ($N_{\text{pix}} = 300$). The last two columns give the adopted distance (S_R) and velocity (S_V) scales based on the $N_{\text{pix}} = 300$ solutions

Model	$N_{\text{pix}} = 200$			$N_{\text{pix}} = 300$			$N_{\text{pix}} = 400$			S_R	S_V
	\tilde{R}_o	φ_o [°]	\mathcal{R}_{\min}^2 [%]	\tilde{R}_o	φ_o [°]	\mathcal{R}_{\min}^2 [%]	\tilde{R}_o	φ_o [°]	\mathcal{R}_{\min}^2 [%]		
m08t4000	9.3	31	0.228	9.5	33	0.342	9.4	38	0.359	0.842	0.900
m12t2000	8.2	23	0.319	8.2	23	0.409	8.2	23	0.337	0.976	0.939
m06t4600	9.6	26	0.388	9.6	26	0.432	9.6	26	0.619	0.833	1.120
m11t2000	8.1	27	0.365	9.0	34	0.467	8.2	28	0.526	0.889	0.964
m08t3200	8.6	24	0.424	9.0	25	0.472	8.7	25	0.515	0.889	0.977
m09t1600	8.5	26	0.341	8.5	26	0.586	8.5	26	0.828	0.941	0.991
m02t2000	8.1	21	0.547	8.1	21	0.628	8.0	23	0.672	0.988	0.946
m03t1000	7.5	22	0.599	9.5	29	0.641	8.0	21	0.728	0.842	1.056
m12t1600	7.3	20	0.557	7.3	19	0.677	7.5	19	0.780	1.096	1.001
m10t1400	7.4	19	0.580	8.1	22	0.709	7.4	15	0.730	0.988	0.916
m04t3000	7.9	18	0.615	7.9	32	0.738	7.7	25	0.784	1.013	0.852
m06t4800	8.0	26	0.675	8.0	25	0.747	9.3	9	0.650	1.000	1.137

Table 4. Several absolute properties of the rescaled B sample models. χ_{loc}^2 : mean square residual between model and observed local properties; σ^D, σ^S : local disc and NS velocity dispersions [km/s]; $\overline{v_\phi^S}$: local NS rotation velocity [km/s]; h_R, h_z : disc scale length [kpc] and local scale height [pc]; Σ_o^D, ρ_o^S : local disc surface density [M_\odot/pc^2] and NS volume density [$10^{-3}M_\odot/\text{pc}^3$]; V_o : local circular velocity [km/s]; Ω_P, R_L : pattern speed of the bar [km/s/kpc] and corotation radius [kpc]; φ_o : bar inclination angle [°]; Υ_K : mass-to-K band luminosity ratio [$M_\odot/L_{K,\odot}$]; τ_0 : microlensing optical depth towards Baade's Window [10^{-6}]. Values in brackets include the DH lenses. The boldfaced models reasonably agree with most of the considered observations

Model	χ_{loc}^2	σ_{RR}^D	$\sigma_{\phi\phi}^D$	σ_{zz}^D	σ_{RR}^S	$\sigma_{\phi\phi}^S$	σ_{zz}^S	$\overline{v_\phi^S}$	h_R	h_z	Σ_o^D	ρ_o^S	V_o	Ω_P	R_L	φ_o	Υ_K	τ_0
m08t4000	2.98	43	28	21	106	117	78	51	2.7	363	47	0.9	195	36	5.5	33	0.60	1.53 (1.75)
m12t2000	1.91	44	27	19	118	107	89	63	4.9	339	49	1.2	200	44	4.5	23	0.68	1.70 (2.12)
m06t4600	5.59	36	26	17	135	129	95	41	4.0	232	58	1.3	230	54	3.9	26	0.59	1.45 (1.61)
m11t2000	1.88	53	26	20	117	116	83	61	2.7	287	40	1.2	210	52	4.0	34	0.57	1.38 (1.48)
m08t3200	3.88	42	25	22	111	124	81	58	2.7	379	44	1.1	214	44	4.8	25	0.72	1.80 (1.97)
m09t1600	3.61	38	24	18	124	121	84	61	4.4	259	50	1.2	212	55	3.9	26	0.73	2.19 (2.33)
m02t2000	1.64	51	29	20	115	117	94	60	3.1	290	43	1.1	210	56	3.9	21	0.73	1.97 (2.07)
m03t1000	2.47	41	30	18	129	125	93	44	4.9	271	45	0.6	216	58	3.9	29	0.53	1.54 (1.89)
m12t1600	3.43	50	30	25	118	115	96	76	3.9	328	70	1.7	217	48	4.6	19	0.96	3.00 (3.13)
m10t1400	1.82	54	28	18	119	111	91	64	5.1	295	47	1.2	198	44	4.9	22	0.70	1.97 (2.18)
m04t3000	3.40	36	24	19	111	106	84	50	3.0	285	39	1.5	200	48	4.3	32	0.72	2.03 (2.11)
m06t4800	2.39	47	27	23	133	133	104	50	4.6	278	58	1.7	229	45	4.6	25	0.79	2.28 (2.46)

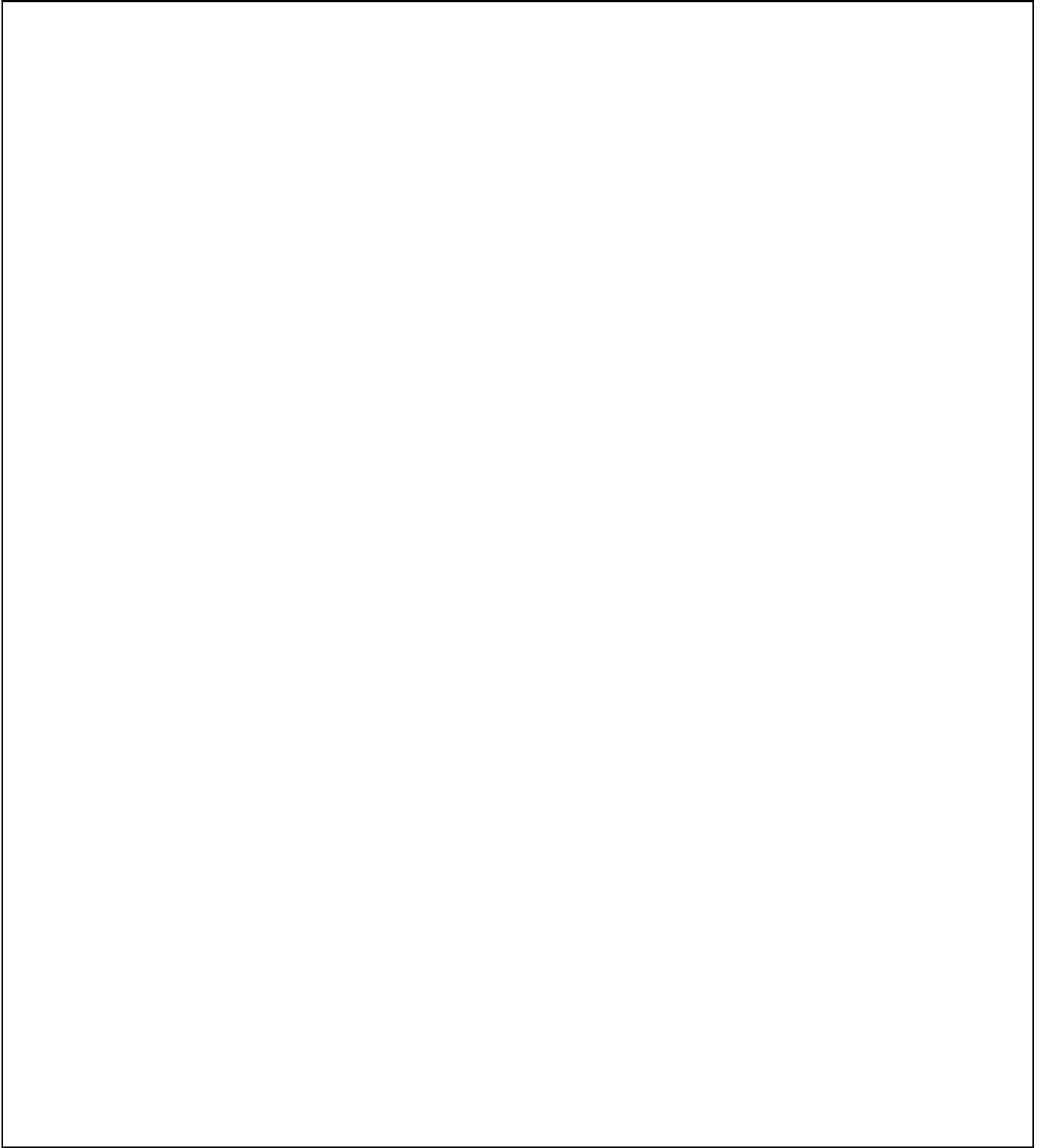


Fig. 10. Comparison of a selection of rescaled models with observations in the bar region. Left: face-on surface density of the visible components; The symbol \odot indicates the location of the observer and the crosses the positions of the Lagrangian points L_1 and L_2 . Rotation is clockwise. Middle: COBE/DIRBE deredened K-band contours (full lines) and corresponding model contours (dashed lines). The b scale is dilated relative to l , hence amplifying the deviations. The region below the horizontal line was excluded in the adjustments because of unreliable extinction correction. The spacing between the contours is 0.5 magnitude in both frames. Right: longitude-velocity diagram of the Galactic HI averaged over $|b| < 1.25^\circ$ and, superposed, the traces of non-self intersecting model x_1 -orbits (dashed lines); the innermost trace represents the cusped x_1 orbit. The model m12t2000 has been symmetrised in all frames. The HI data were kindly provided by H. Liszt and refer to Burton & Liszt (1978)

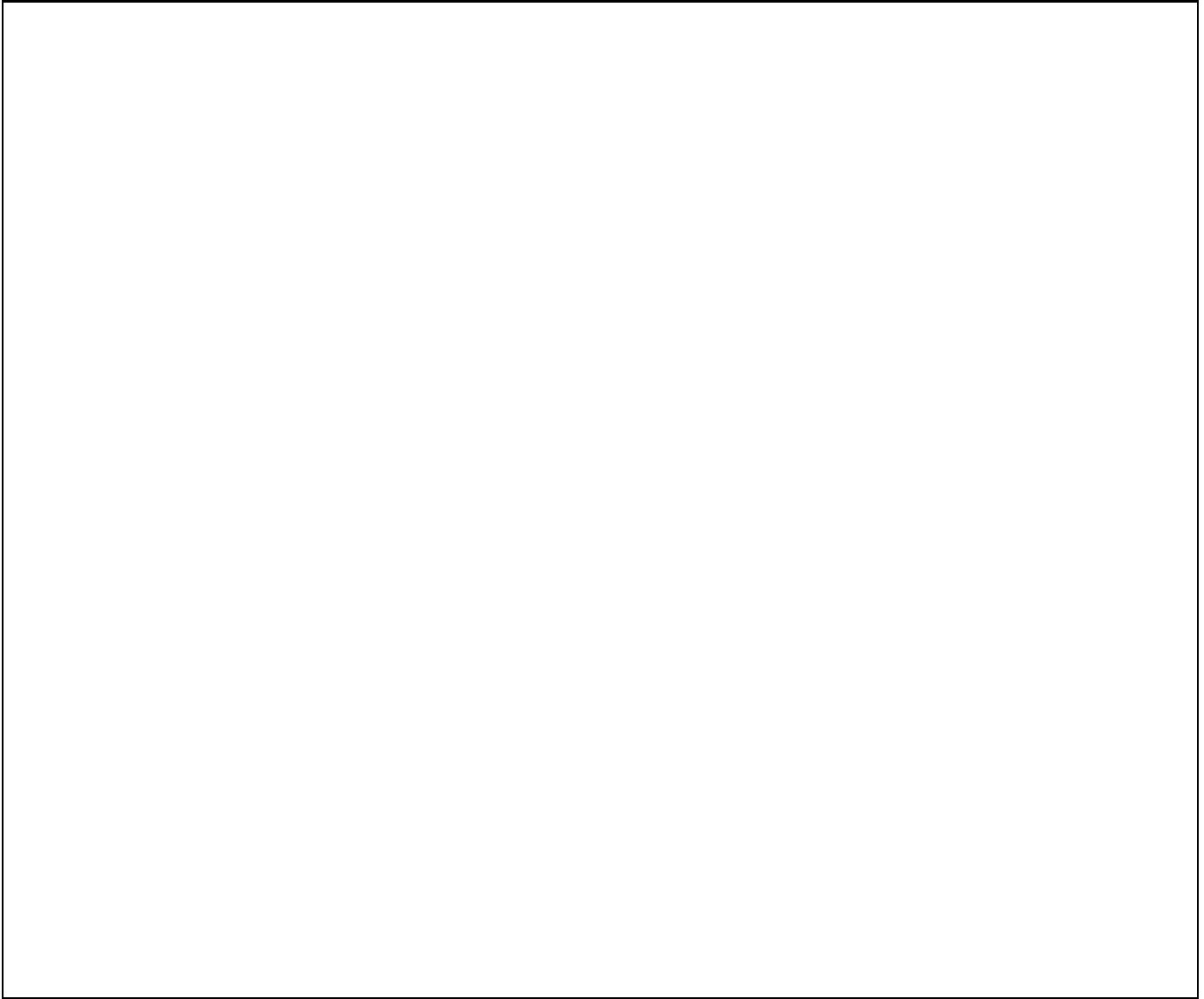


Fig. 10. continued

5. Model properties and discussion

Given the distance scale, there remains only one scale left in the models since the constraint of virial equilibrium links together the distance, velocity and mass scales. We choose here to fix the velocity scale by requiring that the line-of-sight velocity dispersion of the combined NS+disc components towards Baade's Window $(l, b) = (0^\circ 9, -3^\circ 9)$ equals 113 ± 6 km/s, as observed for late-M giants (Sharples et al. 1990), leaving about 10% uncertainty on the absolute mass scale. The resulting velocity scales of the B sample models are listed in Table 3.

The complete scaling of the models allows now to derive several of their absolute properties, which are presented and discussed in this section.

5.1. Local properties

The main local properties of the models, i.e. the properties measured at the location of the observer, are given in Table 4. These include the velocity dispersion of the disc $(\sigma_{RR}^D, \sigma_{\phi\phi}^D, \sigma_{zz}^D)$ and of the NS $(\sigma_{RR}^S, \sigma_{\phi\phi}^S, \sigma_{zz}^S)$, the NS mean rotation velocity $(\overline{v_\phi}^S)$, the disc scale length (h_R) and scale height (h_z) , the disc surface density (Σ_o^D) , the NS volume density (ρ_o^S) and the circular velocity (V_o) .

All quantities, except h_R and V_o , are based on the particles inside a sphere (for the NS) or a vertical cylinder (for the disc) centred on the Sun's position, and hence are not azimuthal averages. The disc scale length is an effective exponential scale length derived from all disc particles within the annulus $0.7 < R/R_o < 1.2$. The circular velocity rests on the azimuthally symmetrised potential.

To quantify the ability of the models to reproduce local observations, Table 4 also gives the mean χ^2 residual between the local model properties, from σ_{RR}^D to Σ_{\circ}^D and excluding h_R , and the corresponding observed values mentioned in Table 2, weighting the contribution of the three disc velocity dispersion components by 1/3 and the four NS velocity moments by 1/4. Models from simulation m07 have very high χ_{loc}^2 due to their small disc scale height, as well as unrealistic mass-to-light ratios and too low microlensing optical depths in Baade’s Window (see Sect. 5.3 and 5.4), and were therefore rejected.

Many models have disc kinematics consistent with observations, and in particular correct ratios between the components of the velocity dispersion. There appears a clear correlation between the vertical velocity dispersion of the disc and its scale height, as expected from self-gravitating isothermal sheets, although not directly depending on the disc surface density. A proper analysis of the disc vertical dynamics would of course require simulations with higher z -resolution. The disc velocity dispersion in model m06t4600 is lower than in m06t4800 because the observer is located farther from the centre (in initial units) and the velocity dispersion decreases outwards.

The velocity dispersion of the NS components is in general similar to that of the local Galactic halo stars, except that its radial anisotropy is insufficient. This difference is probably linked to the initial model truncation at $R_c = 38$ kpc, which limits the amount of radial anisotropy inside the models, and the flatness ($e = 0.5$) of the outer mass distribution, which requires substantial support by azimuthal motion, either in systematic or random form. It is however worthwhile to mention that the local subdwarf kinematics in Table 2 may be biased by selection effects. For example, kinematically selected samples have much larger radial anisotropy than samples selected by metallicity criterions, the velocity dispersion in the latter being even consistent with meridional isotropy (Norris 1987). Moreover, the kinematics of the globular cluster system shows no significant deviation from isotropy.

All models favour $V_{\circ} < 220$ km/s except those from simulation m06. These models have in fact increasing rotation curve from $R_{\circ}/2$ to R_{\circ} , so that our velocity scaling mainly based on the inner region leads to larger circular velocities at R_{\circ} .

5.2. Corotation and terminal velocities from x_1 orbits

An approximate bar pattern speed Ω_P is derived for each model as the least square slope of the bar position angle $\vartheta(t)$ relative to a fixed axis, within a time interval of a few bar rotation and centred on the current time. The related corotation radius R_L then follows from the Lagrangian points L_1 and L_2 , i.e. the saddle points of the effective potential $\Phi_{\text{eff}} = \Phi(R, z) - \frac{1}{2}R^2\Omega_P^2$. Figure 11 plots the sequence generated by our models in the $\Omega_P - R_L$ plane. The B sample values are quantified in Table 2 and the left

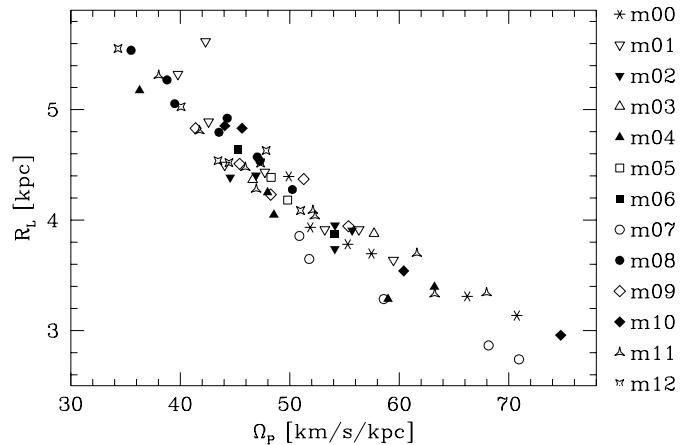


Fig. 11. Corotation radius R_L , derived as the distance of the Lagrangian points L_1 and L_2 to the centre, versus the pattern speed of the bar Ω_P for the A sample models. Each symbol refers to models of the same simulation

frames in Fig. 10 highlight the position of the Lagrangian points. The B sample models have $\Omega_P = 50 \pm 5$ km/s/kpc and $R_L = 4.3 \pm 0.5$ kpc.

These results conflict with the dynamical properties $\Omega_P = 63$ km/s/kpc and $R_L = 2.4 \pm 0.5$ kpc reported by Binney et al. (1991) and are closer to $\Omega_P = 55$ km/s/kpc and $R_L = 3.6$ kpc inferred by Weiner & Sellwood (1996) from SPH gas flow modelling in a rigid potential. The former $\Omega_P - R_L$ pair moreover falls well below the relation displayed in Fig. 11.

Binney et al. (1996) suggest that the peak emission in the COBE near-IR maps at $b = 0$ and near $l \sim -22^\circ$, corresponding to $R \approx 3$ kpc, is due to stars trapped by the Lagrangian point L_4/L_5 . We think that this peak could also arise from star formation in a gaseous pseudo ring, possibly associated with the “expanding 3 kpc arm”, seen tangentially and located close to the inner 4:1 resonance, as the inner rings in many external barred galaxies (Buta 1996 and references therein). According to this picture, corotation would lie significantly beyond 3 kpc.

Moreover, Zhao (1996) has constructed a model for the Galactic bar using Schwarzschild’s technique and imposing $\Omega_P = 60$ km/s/kpc. An N -body evolution of his model shows that this input pattern speed decreases by about 20% after one rotation period (see his Fig. 9), thus becoming consistent with our results.

Binney et al. (1991) have argued that prograde gas in a barred potential, due to the pressure and viscous forces, settles onto the stable and closed orbits of the x_1 family, switching progressively to ever lower energy orbits as long as these develop no loops. Depending on the bar potential, the gas may finally reach a last non-self intersecting, “cusped” x_1 orbit beyond which shocks transform most of the atomic gas into molecular gas, and force the gas to plunge to the more viable orbits of the x_2 family (if

an inner Lindblad resonance exists). Thus, atomic gas is expected to move along non-self intersecting x_1 orbits, providing the key for a model comparison with Galactic HI observations. In particular, the envelop defined by the traces of such orbits in the longitude-velocity l - V diagram should coincide with the observed HI terminal velocities.

Orbits of the x_1 family have been computed in almost all our dynamical models, using the instantaneous frozen potential. Figure 10 shows the comparison of several model x_1 traces versus HI contours in the l - V diagram. Some models reproduce fairly well the HI terminal velocity envelop. The best cases certainly are m04t3000 and m06t4600, which share the common property to arise from simulations with lower disc mass fraction in the bar region: their disc to total mass ratio within $s < 3$ kpc is less than 0.45, where s is the variable defined in Eq. (2). Further cases from the B sample are m12t2000, m08t3200, m09t1600, m02t2000 and m06t4800. All these models, except m06t4800, occur shortly after the formation of the bar, when redistribution of angular momentum has not completely disturbed the initial exponential radial profile of the disc. In general, the presence of the bar tends to steepen the azimuthally averaged inner radial profile of the disc, increasing the central disc surface density.

Most of the models also have x_1 envelopes exceeding the observed terminal velocities, indicating that there could be too much mass near the centre. Such an excess could of course be reduced by increasing the angle φ_0 , but then the peaks of maximum and minimum velocity traced by the cusped x_1 orbit in the l - V diagram would also be shifted towards higher $|l|$. Reducing the velocity scale in general render the local disc kinematics less consistent with observations.

Hence, if the Galactic gas really moves on non self-intersecting closed orbits, then the HI observations suggest that our dynamical models could have too much mass in the disc near the centre.

5.3. Mass-to- K luminosity ratio

In addition to the position of the observer, the COBE-fits in Sect. 4 also yield the K -band mass-to-light ratios Υ_K of the models, without the contribution of the DH component.

Taking $\Upsilon_{K,\odot} = 2.69 \cdot 10^{-12} M_\odot W^{-1} \text{Hz}$ (Wamsteker 1981), the rescaled values for the B sample models range from $\Upsilon_K = 0.53$ to 0.79 in Solar units, except for model m12t1600 (see Table 2). The total NS+disc+DH mass of the B sample models within the spheroid $s < 3$ kpc is $(2.6 \pm 0.15) \times 10^{10} M_\odot$, with about 8% contribution from the DH component. This gives an average percentage by which Υ_K is underestimated.

Modelling the gas dynamics of the barred galaxy M100 (NGC4321), which has a Hubble type similar to the Milky Way, Knapen et al. (1995) have inferred $\Upsilon_K > 0.7$ outside its nuclear ring. Moreover, for stellar populations with

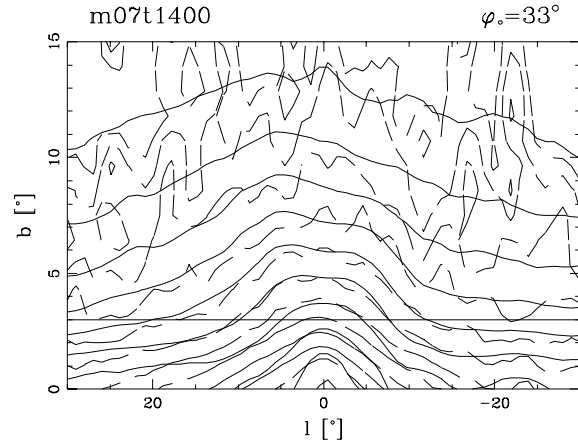


Fig. 12. Confrontation of a model with small h_z/R_0 to the COBE data. The caption is similar to Fig. 10

near-IR emission dominated by late K and M giants, as for the Galactic bulge (Arendt et al. 1994), similar mass-to-light ratios are expected (Worthey 1994). Such lower limit for Υ_K rules out some models, like those of simulation m07 which all have $\Upsilon_K < 0.4$. The substantial microlensing optical depths towards the Galactic bulge also argue for a large value of Υ_K , as discussed below in Sect. 5.4.

A noticeable difference between the COBE K -band map and the model maps in Fig. 10 is that the model contours are steeper in the low latitude and $|l| \gtrsim 15^\circ$ region, i.e. where the disc becomes dominant. Even if our correction for extinction fails at $b \lesssim 3^\circ$, the near-IR contours in this region still remain very flat after more elaborated dust subtraction of the COBE data (Spergel et al. 1997) and hence the difference is probably real. Several reasons may lead to this departure.

First, the Galactic disc scale height may be lower by a factor ~ 2 in the inner Galaxy than in the Solar neighbourhood, as deduced by Kent et al. (1991) from the Spacelab IR Telescope data and by Binney et al. (1996) from the deprojection of the COBE L -band map. At constant surface density, discs with smaller scale height are more concentrated towards the plane and should therefore contribute more to the low latitude near-IR emission. Our models, started with radially constant disc thickness, do not present such large disc scale height gradient outside the bar region. But models from simulation m07 (see Fig. 12), with the thinnest disc, indeed have flatter l - b contours than models from m08. The variable scale height alternative however is not supported by observations in external late-type spiral galaxies (de Grijs & van der Kruit 1996 and reference therein).

Second, discs with more foreground mass between the bulge and the observer will also enhance the low latitude integrated light. This is the case for the m06 models (Fig. 10). At fixed total disc mass, because of the higher initial disc scale length, these models have higher disc sur-

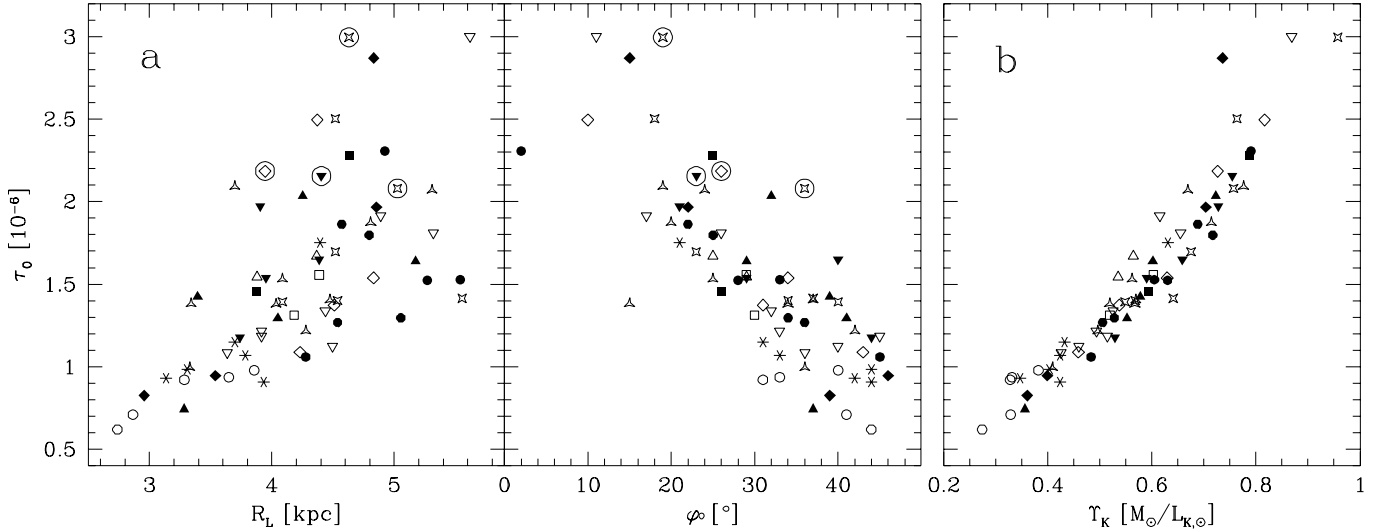


Fig. 13. **a** Dependence of the microlensing optical depths τ_0 (without DH contribution) towards Baade’s Window on the corotation radius R_L , which is a reasonable indicator of the radial extension of the bar, and on the bar inclination angle φ_0 , for the A sample models. The encircled points indicate models with prominent spiral structures. **b** Relation between τ_0 and the mass-to-light ratio Υ_K for the same models. The symbols are as in Fig. 11

face density in the outer region, including the first few kpc below R_0 . Increasing simply the disc mass is less efficient because the inner disc, mixing with the NS component during the bar instability, will also contribute more to the bulge emission.

Finally, the assumption $\Upsilon_K = \text{const.}$ may not hold close to the Galactic plane because of near-IR emission from interstellar matter, or recent star formation. In the latter case, red supergiants, too young for having diffused as far above the plane as the old disc population, could significantly contribute to the K -emission and reduce Υ_K at low Galactic latitude. However our COBE-adjustments should not be affected by such a Υ_K gradient since the region $|b| < 3^\circ$ was excluded. Alternatively, the IR mass-to-light ratio could also be lower in the Galactic disc than in the bulge, as found by Verdes-Montenegro et al. (1995) for NGC7217 in the I -band.

In the next section, we will argue for the massive disc possibility and against a variable disc scale height.

5.4. Bulge microlensing

The microlensing optical depths τ towards the galactic bulge provide a serious direct probe of the mass distribution inside the Solar circle.

The first results obtained by the OGLE and MACHO experiments favour surprisingly large optical depths: the reported values are *at least* $(3.3 \pm 1.2) \times 10^{-6}$ for 9 bulge stars essentially located in Baade’s Window (Udalski et al. 1994), and $(3.9^{+1.8}_{-1.2}) \times 10^{-6}$ for 13 clump giants with mean Galactic coordinates $l = 2^\circ 55$ and $b = -3^\circ 64$ (Alcock et al. 1997), whereas axisymmetric models predict values less than 10^{-6} (Evans 1994 and references therein). The

contribution of bulge lenses may however significantly increase the model predictions if the bulge is an elongated bar seen nearly end-on (Evans 1994, Kiraga & Paczynski 1994, Zhao et al. 1996, Zhao & Mao 1996).

We have computed the model microlensing optical depths towards Baade’s Window, averaged over all sources along the line-of-sight, from the following Monte Carlo version of Eq. (5) given by Kiraga & Paczynski (1994):

$$\tau_{\beta_s} = \frac{4\pi G}{\Delta\Omega c^2} \left[\sum_{D_s} \sum_{D_d < D_s} \left(\frac{m_d}{D_d} - \frac{m_d}{D_s} \right) D_s^{2\beta_s} \right] \left[\sum_{D_s} D_s^{2\beta_s} \right]^{-1} \quad (20)$$

where the outer sums involve all source particles within a solid angle $\Delta\Omega$ of the selected direction and the inner sum all lens particles in the same solid angle between the specified source and the observer, the symbols D_s and D_d referring resp. to the source and lens distances relative to the observer, and m_d to the mass of the lens particles. G is the gravitational constant, c the speed of light and β_s the parameter introduced by Kiraga & Paczynski (1994) to describe the detection probability of the sources: $\beta_s = 0$ if the sources are detectable whatever their distance, like clump giant stars, and $\beta_s \approx -1$ for main sequence stars (Bissantz et al. 1996 and references therein).

Optical depths are calculated with and without including DH lenses. Table 4 gives some results for $\beta_s = 0$. The optical depths for other values of β_s are almost proportional to τ_0 : in particular, we find $\tau_{-1} \approx \frac{2}{3}\tau_0$, both with or without DH lenses. The DH contributes roughly 9% to the total optical depth. In the mean direction of the Alcock et al. (1997) fields, τ_0 is on the average 15% higher than in Baade’s Window, in agreement with the above reported observations.

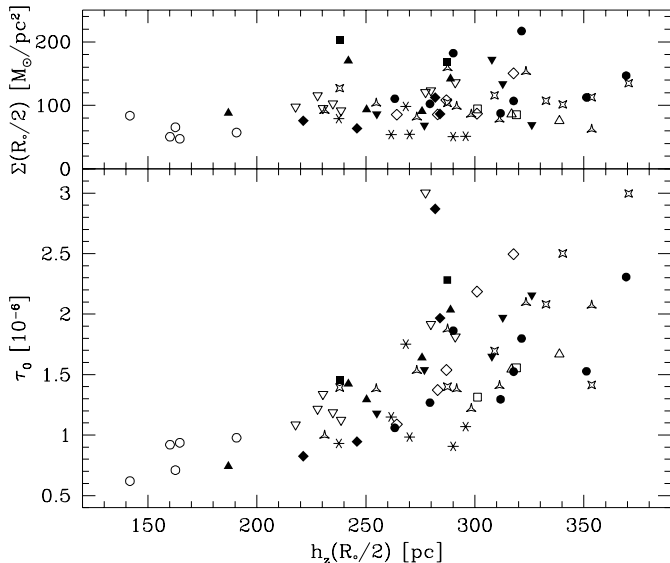


Fig. 14. Microlensing optical depths τ_0 (without DH) towards Baade’s Window versus disc scale height half way between the observer and the Galactic centre for the A sample models. The upper frame shows that the correlation is not induced by a variable disc surface density. The symbols are as in Fig. 11

Figure 13a shows the optical depths of the A sample models towards Baade’s Window as a function of the size of the bar and its inclination angle relative to the observer. The optical depth strongly depends on φ_o , increasing from $\tau_0 \sim 10^{-6}$ for $\varphi_o = 40^\circ$ to $\tau_0 \sim 2.5 \times 10^{-6}$ for $\varphi_o = 15^\circ$, and is roughly proportional to R_L . The dispersion in each plot partly reflects the dependence of the optical depth on both φ_o and R_L : at fixed R_L , the larger values of τ_0 come from models with more end-on bars.

Clearly, the optical depths depends on the mass scaling and thus on the adopted mass-to-light ratio Υ_K , as depicted in Fig. 13b. Within the various investigated models, this relation does not seem to depend much on a third parameter. According to it, the 1σ lower limit of the observed optical depths, $\tau \gtrsim 2.1 \times 10^{-6}$, implies $\Upsilon_K > 0.7$, consistent with the previous discussion on this parameter (Sect. 5.3).

If more event statistics confirm the large observed optical depths, then the models in Fig. 13a with our best COBE-estimate $28^\circ \pm 7^\circ$ for the bar inclination angle are inconsistent with the microlensing constraints. This could indicate that our models have insufficient mass along the line-of-sight in Baade’s Window. To enhance that mass without increasing the x_1 -terminal velocities, an obvious possibility is to increase the disc mass outside the bar region at the expense of the DH, i.e. approaching a maximum disc solution, as suggested by Alcock et al. (1997) and by the recent Galactic structure review of Sackett (1997). If dark matter in the outer Galaxy is in molecular form (Pfenniger et al. 1994) and thus concentrated in the plane, its contribution to the squared inner circular

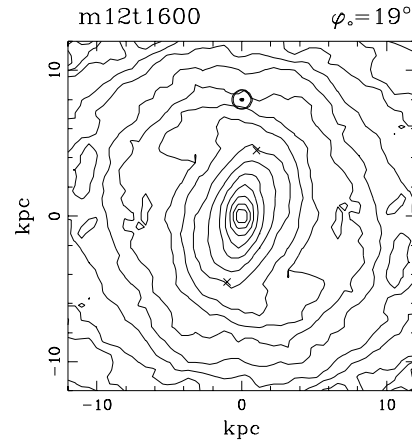


Fig. 15. Face-on view of a model with optical depth towards Baade’s Window over 3×10^{-6} . The caption is similar to Fig. 10 and the model has been symmetrised

velocity can become *negative*, even allowing for an over maximum disc solution. To ensure a low central surface density, such a heavy disc would then have to be partially hollow relative to its exponential extrapolation inside the bulge.

Microlensing optical depths towards Baade’s Window also depend on the disc scale height. At fixed surface density and distance z_1 above the plane, one can show that the (exponential) scale height which maximises the volume density is $h_z = z_1$ if the vertical mass distribution is exponential. Furthermore, the lenses which most contribute to the optical depth are those lying half way between the source and the observer and, for reasonable disc parameters, the mass density along Baade’s Window is about constant (e.g. for $h_R = 3.5$ kpc and $h_z(R) = \text{const.} = 240$ pc). Thus for bulge sources, the maximum disc contribution in this window should come from stars at $R = 4-5$ kpc, which are about 270 pc away from the plane. Our models indeed produce larger values of τ_0 on the average when $h_z(R_o/2) \approx 300$ pc, as shown in Fig. 14. In particular, models with $h_z \lesssim 250$ pc in the inner part all have $\tau_0 < 1.5 \times 10^{-6}$, hard to conceal with observations. From this we infer that the mass distribution of the Galactic disc probably has a constant scale height between $\sim R_o/2$ and R_o , contrary to the constant mass-to-light ratio interpretations of near-IR surface photometry data (Kent et al. 1991; Binney et al. 1996).

The effect of asymmetries like spiral arms may also affect the optical depths towards the bulge, as illustrated in Fig. 13a. Model m12t1600 has one of the largest τ_0 towards Baade’s Window and indeed exhibits a strong spiral structure (see Fig. 15). Another example, with larger φ_o and smaller R_L , is m09t1600 (see Fig. 10). The orientation of the Galactic bar is such that the line-of-sight through Baade’s Window crosses the spiral arm starting at the near end of the bar almost tangentially and at a distance

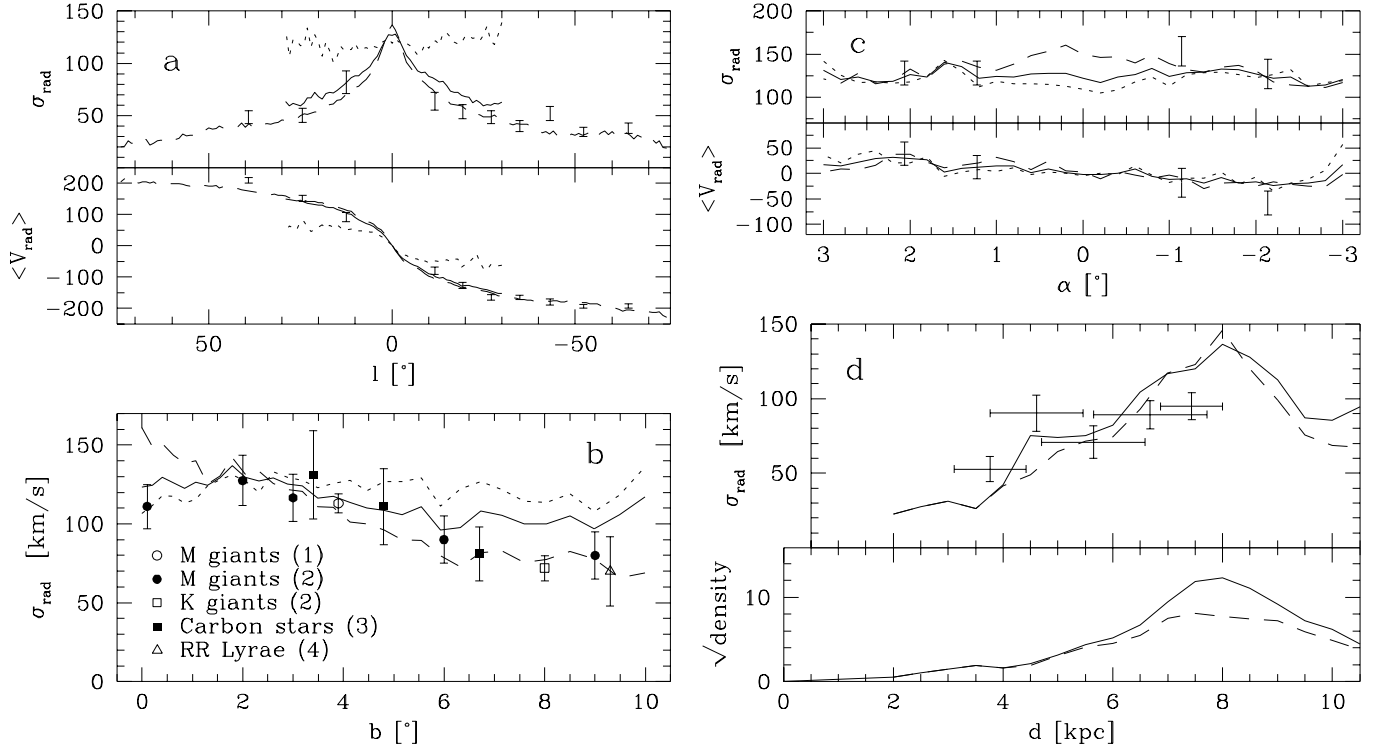


Fig. 16a-d. Galactocentric radial kinematical properties of the model m08t3200. In all plots, the dashed, dotted and full lines stand resp. for disc, NS and disc+NS particles. **a** Radial velocity dispersion and mean velocity within $|b| < 5^\circ$ based on particles interior to the Solar circle. The points with error bars are derived from the te Lintel Hekkert et al. (1991) catalogue of double peaked OH/IR stars. **b** Projected radial velocity dispersion along the bar minor axis ($l = 0$). The data are from: (1) Sharples et al. 1990; (2) Terndrup published by Rich 1996; (3) Tyson & Rich 1991; (4) Rodgers 1977. **c** Projected radial velocity moments along an axis through the Galactic centre and inclined by 55° relative to the minor axis, and the corresponding Blum et al. (1995) M giant observations. The angle α is measured with respect to $l = b = 0$ and has the same sign as l . **d** Radial velocity dispersion in Baade’s Window as a function of the distance d from the observer, with the K giant data of Lewis & Freeman (1989). The lower plot also represents the square root of the relative mass distribution per solid angle along the line-of-sight (arbitrary units)

where microlensing should be very efficient. The gain in optical depth is of order 0.5×10^{-6} .

5.5. Inner kinematics

It is beyond the scope of this paper to study the detailed kinematics of all the dynamical models. Instead, we present here the case of a single model, m08t3200, which is in fair agreement with almost all explored constraints. In Figs. 16a-d, several kinematical predictions of this model are compared to stellar observations.

The agreement between the longitudinal kinematics of the model disc and that of the OH/IR stars (Fig. 16a) is very convincing. The model particles outside the Solar circle were not taken into account as the data contain only very few OH/IR stars at $|l| > 90^\circ$. No velocity moment has been derived from the data within $|l| < 10^\circ$ because in this region the radial velocity dispersion depends non-negligibly on the galactic latitude and the te Lintel Hekkert et al. (1991) OH/IR stars severely suffer from undersampling at $b \lesssim 2^\circ$.

The minor axis velocity dispersion of the model (Fig. 16b) is different for the NS and disc components. The observed kinematics are best traced by the NS component near the centre and by the disc component at large Galactic latitude. In the Blum et al. (1995) fields, the kinematics of these components are more similar (Fig. 16c).

The velocity dispersion in Baade’s Window as a function of the distance from the observer is close to that observed for K giants (Fig. 16d), except near the tangent point. However, the projected velocity dispersion of these stars is obviously less than the 113 km/s of the M giants which was used to scale the model. Furthermore, the distance distribution of the foreground model particles is roughly proportional to d^2 , whereas the distribution of the K giants seems nearly linear with d (Sadler et al. 1996), suggesting that the latter may be biased towards the near stars. This difference between model and observations is hardly due to a variable Galactic disc scale height. One can indeed show that, within 3–4 kpc from the observer, the simulated line-of-sight mass distribution towards Baade’s Window in a realistic analytical double exponential disc is

Table 5. Comparison of model m08t3200 versus K giant projected radial kinematics in off axis bulge fields. Boldfaced, italic and roman velocities refer resp. to disc, NS and disc+NS particles. The mean velocities are Galactocentric. The references for the observations are Harding 1996, Minniti 1996a, Minniti 1996b and Minniti et al. 1992

			Observations		Model	
l [°]	b [°]	[Fe/H]	σ_r	$\overline{v_r}$	σ_r	$\overline{v_r}$
-10.0	-10.0	> -1	67 ± 6	-82 ± 8	72	-81
		< -1	107 ± 6	-37 ± 8	<i>120</i>	<i>-41</i>
		all	–	–	110	-71
9.9	-7.6	> -1	70 ± 7	56 ± 10	70	92
		< -1	91 ± 13	-18 ± 18	<i>117</i>	<i>40</i>
		all	–	–	99	66
8.0	7.0	> -1	72 ± 4	66 ± 5	77	68
		< -1	109 ± 10	-7 ± 14	<i>121</i>	<i>36</i>
		all	–	–	100	54
12.0	3.0	–	–	–	75	111
		–	–	–	<i>124</i>	<i>45</i>
		all	68 ± 6	77 ± 9	93	96

very similar for a radially constant or a linearly increasing h_z if the face-on surface density profile is kept the same.

Table 5 reviews some off-axis K giant observations and give the corresponding model predictions. The velocity moments of the model disc component resemble those of the giants with $[\text{Fe}/\text{H}] > -1$. The l – b proper motion dispersions of the model in Baade’s Window are $(\sigma_{\mu_l}, \sigma_{\mu_b}) = (3.15, 2.38)$ m''/yr for the disc, $(2.96, 2.81)$ m''/yr for the NS and $(3.08, 2.57)$ m''/yr for both visible components together, whereas the observed values for K giants are $(3.2 \pm 0.1, 2.8 \pm 0.1)$ m''/yr (Spaenhauer et al. 1992).

6. Conclusion

We have built many self-consistent 3D dynamical barred models of the Milky Way extending beyond $R = R_\odot$ by N -body integration of various bar unstable axisymmetric models. The models, extracted from the simulations at a frequency of 200 Myr, include 3 components: a nucleus-spheroid standing for the Galactic inner bulge and stellar halo, a disc mainly representing the Galactic old disc and a non-dissipative dark halo. The comparison of the models with observational constraints leads to the following considerations.

1) The spatial location of the observer in each model is constrained by the COBE/DIRBE K -band map corrected for extinction by dust, assuming a constant mass-to-light ratio Υ_K for the luminous mass components. The results for the best matching models, with mean quadratic residuals between model and data fluxes down to 0.3%, suggest that the angle between the $l = b = 0$ line and the major axis of the Galactic bar is $28^\circ \pm 7^\circ$.

2) Scaling the models such as the distance of the observer to the centre is $R_\odot = 8$ kpc and the projected radial velocity dispersion towards Baade’s Window 113 km/s, as

observed for M giants, absolute model properties are derived. A dozen of models reproduce fairly well both the COBE-data and observations in the Solar Neighbourhood, although with a rather low radial versus azimuthal velocity dispersion anisotropy of the spheroid components.

3) The bars in these models have a face-on axis ratio $b/a = 0.5 \pm 0.1$ and a pattern speed $\Omega_P = 50 \pm 5$ km/s/kpc, placing the corotation at 4.3 ± 0.5 kpc. Models with a disc mass fraction below 0.45 within 3 kpc from the centre produce envelopes of non self-intersecting x_1 -orbits in the l – V diagram which better agree with the observed HI terminal velocities.

4) The microlensing optical depths of the models towards the bulge strongly depends on the bar inclination angle φ_\odot , increasing from $\tau_0 \sim 10^{-6}$ for $\varphi_\odot = 40^\circ$ to $\tau_0 \sim 2.5 \times 10^{-6}$ for $\varphi = 15^\circ$ towards Baade’s Window, whereas observations rather support values over 3×10^{-6} . We find that a spiral arm starting at the near end of the bar can increase the optical depths by 0.5×10^{-6} and thus reduce the gap between model and observed values.

5) All models with a disc scale height $h_z \leq 250$ pc half way between the observer and the Galactic centre have $\tau_0 < 1.5 \times 10^{-6}$, arguing against an inwards decreasing disc scale height. This result is also in agreement with the constant h_z observed in late-type spirals.

6) The models predict a mass-to- K luminosity ratio $\Upsilon_K = 0.6$ – 0.8 in Solar units. Values near the upper limit are consistent with the mass-to-light ratio estimated for M100 (NGC4321), a galaxy similar to the Milky Way, and favour microlensing optical depths closer to the observed values. There is indeed an obvious but tight correlation between τ_0 and Υ_K , according to which $\tau_0 \gtrsim 2 \times 10^{-6}$ implies $\Upsilon_K > 0.7$.

7) Most models predict too low surface brightness relative to the COBE-data in the region $|l| \lesssim 15^\circ$ dominated by the disc. Beside an improbable lower disc scale height in the inner Galaxy, or a variable mass-to-light ratio, this discrepancy could indicate that the Galactic disc outside the bar region is more massive than assumed in the models, favouring large microlensing optical depths and arguing for a maximum disc Milky Way.

8) The disc radial kinematics of the models resembles the observed kinematics of K giants with $[\text{Fe}/\text{H}] > -1$ in the outer bulge.

As reasonable models regarding most observational constraints, we would recommend the models m08t3200 and m04t3000.

Acknowledgements. I would like to thank L. Martinet and D. Pfenniger for many enlightening discussions and for critical reading of the paper, as well as J. Sellwood for refering this paper and D. Pfenniger for providing its efficient N -body code. This work has been partially supported by the Swiss National Science Foundation.

Appendix A: a non-Gaussian bounded 3D distribution

A convenient 3D distribution with non-zero probability over a finite volume, i.e. avoiding the tails of the multi-normal distribution, is given by:

$$B_3(\xi, \eta, \zeta) = [2^{\kappa+\lambda-1} B(\kappa, \lambda) B(\frac{1}{2}, \mu) B(\frac{1}{2}, \omega)]^{-1}.$$

$$\begin{cases} (1+\xi)^{\kappa-2}(1-\xi)^{\lambda-2}(1-\frac{\eta^2}{1-\xi^2})^{\mu-\frac{3}{2}}(1-\frac{\zeta^2}{1-\xi^2-\eta^2})^{\omega-1} & \text{if } \xi^2 + \eta^2 + \zeta^2 \leq 1 \\ 0 & \text{otherwise,} \end{cases} \quad (\text{A1})$$

where B is the Beta function, and κ , λ , μ and ω are four parameters. In the reduced variables ξ , η and ζ , this distribution is bounded by a sphere of radius 1 on which, as long as $\kappa, \lambda > 2$, $\mu > 3/2$ and $\omega > 1$, it continuously vanishes. If $\kappa = \lambda = 2$, $\mu = 3/2$ and $\omega = 1$, the distribution is homogeneous inside the boundary sphere and smaller values of these parameters produce singularities on it.

The first and second moments are:

$$\bar{\eta} = \bar{\zeta} = \overline{(\xi - \bar{\xi})\eta} = \overline{(\xi - \bar{\xi})\zeta} = \bar{\eta}\bar{\zeta} = 0, \quad (\text{A2})$$

$$\bar{\xi} = \frac{\kappa - \lambda}{\kappa + \lambda}, \quad (\text{A3})$$

$$\sigma_{\xi\xi}^2 \equiv \overline{(\xi - \bar{\xi})^2} = 4 \frac{\kappa\lambda}{(\kappa + \lambda)^2(\kappa + \lambda + 1)}, \quad (\text{A4})$$

$$\sigma_{\eta\eta}^2 \equiv \overline{\eta^2} = \frac{4}{2\mu + 1} \frac{\kappa\lambda}{(\kappa + \lambda)(\kappa + \lambda + 1)}, \quad (\text{A5})$$

$$\sigma_{\zeta\zeta}^2 \equiv \overline{\zeta^2} = \sigma_{\eta\eta}^2 \cdot \frac{2\mu}{2\omega + 1}. \quad (\text{A6})$$

Depending on κ and λ , the distribution is skewed in ξ , the maximum of probability lying at:

$$\xi_{\max} = \frac{\kappa - \lambda}{\kappa + \lambda - 4}. \quad (\text{A7})$$

Figure A1 displays an example of the 2D distribution B_2 obtained after integrating B_3 over ζ :

$$\begin{aligned} B_2(\xi, \eta) &\equiv \int B_3(\xi, \eta, \zeta) d\zeta \\ &\propto (1+\xi)^{\kappa-3/2}(1-\xi)^{\lambda-3/2} \left(1 - \frac{\eta^2}{1-\xi^2}\right)^{\mu-1} \end{aligned} \quad (\text{A8})$$

The inversion of Eqs. (A3)-(A6) provides the parameters of the B_3 -distribution as a function of the aimed moments:

$$\kappa = \frac{1}{2} \frac{(1 + \bar{\xi})(1 - \bar{\xi}^2 - \sigma_{\xi\xi}^2)}{\sigma_{\xi\xi}^2}, \quad (\text{A9})$$

$$\lambda = \frac{1}{2} \frac{(1 - \bar{\xi})(1 - \bar{\xi}^2 - \sigma_{\xi\xi}^2)}{\sigma_{\xi\xi}^2}, \quad (\text{A10})$$

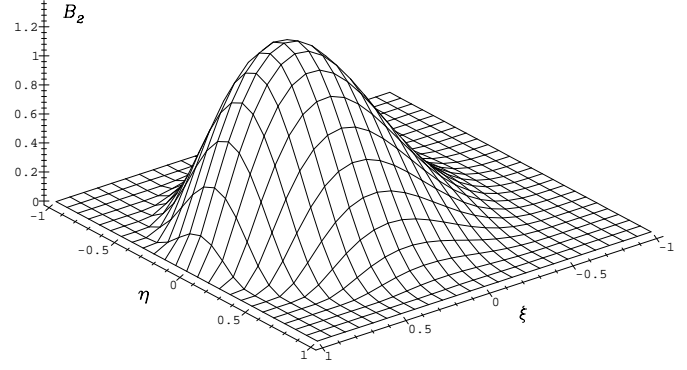


Fig. A1. Distribution of the variables ξ and η resulting from Eq. (A8), with $\kappa = 5$, $\lambda = 3$ and $\mu = 4$

$$\mu = \frac{1}{2} \frac{1 - \bar{\xi}^2 - \sigma_{\xi\xi}^2 - \sigma_{\eta\eta}^2}{\sigma_{\eta\eta}^2}, \quad (\text{A11})$$

$$\omega = \frac{1}{2} \frac{1 - \bar{\xi}^2 - \sigma_{\xi\xi}^2 - \sigma_{\eta\eta}^2 - \sigma_{\zeta\zeta}^2}{\sigma_{\zeta\zeta}^2}. \quad (\text{A12})$$

To generate random numbers distributed according to B_3 , one may use the property that:

$$t_\xi \equiv \frac{1}{2}(\xi + 1), \quad (\text{A13})$$

$$t_\eta \equiv \frac{1}{2} \left(\frac{\eta}{\sqrt{1-\xi^2}} + 1 \right), \quad (\text{A14})$$

$$t_\zeta \equiv \frac{1}{2} \left(\frac{\zeta}{\sqrt{1-\xi^2-\eta^2}} + 1 \right) \quad (\text{A15})$$

follow Beta distributions with parameters κ, λ for t_ξ , γ, γ for t_η , and ω, ω for t_ζ .

Appendix B: the \mathcal{R}^2 residual

If the model fluxes are decomposed into $F_i = F_{i,1} + F_{i,2}$, where $F_{i,1}$ is the exact part and $F_{i,2}$ is the statistical error due to the finite number of particles, the χ^2 in Eq. (16) expands into:

$$\begin{aligned} \chi^2 &= \sum_{i=1}^{N_{\text{pix}}} \frac{(F_{i,1} - F_i^\circ)^2}{\sigma_i^2} \\ &+ \sum_{i=1}^{N_{\text{pix}}} \frac{F_{i,2}^2}{\sigma_i^2} + 2 \sum_{i=1}^{N_{\text{pix}}} \frac{F_{i,2}(F_{i,1} - F_i^\circ)}{\sigma_i^2}. \end{aligned} \quad (\text{B1})$$

The expected value of the second term in the right hand side, when resulting from a fit, is the number of degree of freedom ν (if the errors were Gaussian, then this term would follow the standard χ^2 statistics), whereas the last term is about zero since by definition the $F_{i,2}$'s must van-

ish on the average. With these simplifications, the best estimate of the function:

$$\mathcal{R}^2 \equiv \left[\sum_{i=1}^{N_{\text{pix}}} \frac{1}{\sigma_i^2 / F_i^{\circ 2}} \right]^{-1} \sum_{i=1}^{N_{\text{pix}}} \frac{[(F_{i,1} - F_i^{\circ}) / F_i^{\circ}]^2}{\sigma_i^2 / F_i^{\circ 2}}, \quad (\text{B2})$$

i.e. the quadratic relative residuals between the $F_{i,1}$'s and the F_i° 's averaged over pixels and weighted by the inverse of the relative variance, indeed reduces to Eq. (15).

Appendix C: the variance of the model fluxes

The model flux in a given pixel is of the form:

$$F(\mathbf{D}) = \sum_{k=1}^N f(D_k), \quad (\text{C1})$$

where N is the total number of particles in the pixel, the D_k 's are the distances of the particles relative to the observer and $\mathbf{D} \equiv (D_1, \dots, D_N)$. Noting resp. $P(N)$ and $p(D)$ the distributions of N and of the distances, the two first moments of F are:

$$\begin{aligned} \overline{F^n} &\equiv \sum_{N=0}^{\infty} P(N) \cdot \int_0^{\infty} dD_1 p(D_1) \dots \int_0^{\infty} dD_N p(D_N) F(\mathbf{D})^n \\ &= \begin{cases} \overline{N} \cdot \overline{f} & n = 1 \\ \overline{N} \overline{f^2} + (\overline{N} \overline{f})^2 & n = 2, \end{cases} \quad (\text{C2}) \end{aligned}$$

where

$$\overline{N} = \sum_{N=0}^{\infty} N P(N), \quad (\text{C3})$$

$$\overline{f^n} = \int_0^{\infty} p(D) f(D)^n dD \quad n = 1, 2. \quad (\text{C4})$$

The result for $n = 2$ in Eq. (C2) requires the assumption that the first and second moments of P are identical, which is true for Poisson statistics. Hence the variance of F becomes:

$$\sigma^2(F) = \overline{F^2} - \overline{F}^2 = \overline{N} \cdot \overline{f^2} \approx \sum_{k=1}^N f(D_k)^2. \quad (\text{C5})$$

References

- Alcock C., Allsman R.A., Alves D. et al. 1997, ApJ 479, 119
Arendt R.G., Berriman G.B., Boggess N. et al. 1994, ApJ 425, L85
Athanassoula E., Sellwood J.A. 1986, MNRAS 221, 213
Bacon R., Simien F., Monnet G. 1983, A&A 128, 405
Bahcall J.N., Schmidt M., Soneira R.M. 1983, ApJ 265, 730
Becklin E.E., Neugebauer G. 1968, ApJ 151, 145
Beers T.C., Sommer-Larsen J. 1995, ApJS 96, 175
Binney J., Gerhard O., Spergel D. 1996, preprint astro-ph/9609066, submitted to MNRAS
Binney J., Gerhard O.E., Stark A.A., Bally J., Uchida K.I. 1991, MNRAS 252, 210
Binney J., Tremaine S. 1987. In: Ostriker J.P. (Ed.) Galactic Dynamics. New Jersey, Princeton Univ. Press, p. 120
Bissantz N., Englmaier P., Binney J., Gerhard O. 1996, preprint astro-ph/9612026, submitted to MNRAS
Blum R.D., Carr J.S., Sellgren K., Terndrup D.M. 1995, ApJ 449, 623
Burton W.B., Liszt H.S. 1978, ApJ 225, 815
Buta R. 1996. In: Buta R., Crocker D.A., Elmegreen B.G. (eds.) Proc. IAU Coll. 157, Barred Galaxies. ASP Conf. Ser. 91, p. 11
Caldwell J.A.R., Ostriker J.P. 1981, ApJ 251, 61
de Grijs R., van der Kruit P.C. 1996, A&AS 117, 19
de Vaucouleurs G. 1964. In: Kerr F.J., Rodgers A.W. (eds.) Proc. IAU-URSI Symp. 20, The Galaxy and the Magellanic Clouds. Canberra, Aust. Acad. Sci., p. 88
Durand S., Dejonghe H., Acker A. 1996, A&A 310, 97
Dwek E., Arendt R.G., Hauser M.G. et al. 1995, ApJ 445, 716
Evans N.W. 1994, ApJ 437, L31
Friedli D., Benz W. 1993, A&A 268, 65
Fux R. 1997, PhD thesis, Geneva University
Fux R., Martinet L. 1994, A&A 287, L21
Fux R., Martinet L., Pfenniger D. 1996. In: Blitz L., Teuben P. (eds.) Proc. IAU Symp. 169, Unsolved problems of the Milky Way. Dordrecht, Kluwer, p. 125
Gerhard O. 1996. In: Blitz L., Teuben P. (eds.) Proc. IAU Symp. 169, Unsolved problems of the Milky Way. Dordrecht, Kluwer, p. 79
Gyuk G. 1996, preprint astro-ph/9607134
Harding P. 1996. In: Morrison H., Sarajedini A. (eds.) Formation of the Galactic halo inside and out. ASP Conf. Ser. 92, p. 151
Hernquist L. 1993, ApJS 86, 389
Kent S.M. 1992, ApJ 387, 181
Kent S.M., Dame T.M., Fazio G. 1991, ApJ 378, 131
Kiraga M., Paczynsky B. 1994, ApJ 430, L101
Knapen J.H., Beckman J.E., Heller C.H., Shlosman I., De Jong R.S. 1995, ApJ 454, 623
Kuijken K. 1995, ApJ 446, 194
Kuijken K. 1996. In: Buta R., Crocker D.A., Elmegreen B.G. (eds.) Proc. IAU Coll. 157, Barred Galaxies. ASP Conf. Ser. 91, p. 504
Kuijken K., Dubinski J. 1995, MNRAS 277, 1341
Kuijken K., Gilmore G. 1989, MNRAS 239, 605
Lewis J.R., Freeman K.C. 1989, AJ 97, 139
Majewski S.R. 1993, ARA&A 31, 575
Matsumoto T., Hayakawa S., Koizumi H. et al. 1982. In: Riegler G., Blandford R. (eds.) The Galactic Center. New York: AIP, p. 48
Mihalas D., Binney J., 1981. In: Galactic astronomy. San Francisco, Freeman Company, p. 525
Minniti D. 1996a, AJ 112, 590
Minniti D. 1996b, ApJ 459, 579
Minniti D., White S.D.M., Olszewski E.W., Hill J.M. 1992, ApJ 393, L47
Miyamoto M., Nagai R. 1975, Publ. Astron. Soc. Japan 27, 533
Mulder W.A., Liem B.T. 1986, A&A 157, 148
Norris J. 1987. In: Gilmore G., Carswell B. (eds) The Galaxy. Dordrecht, Reidel, p. 297
Pfenniger D., Combes F., Martinet L. 1994, A&A 285, 79

- Pfenniger D., Friedli D. 1993, *A&A* 270, 561
- Preston G.W., Shectman S.A., Beers T.C. 1991, *ApJ* 375, 121
- Rich R.M. 1996. In: Morrison H., Sarajedini A. (eds.) Formation of the Galactic halo inside and out. ASP Conf. Ser. 92, p. 24
- Rieke G.H., Lebofsky M.J. 1985, *ApJ* 288, 618
- Rix H.W., Zaritsky D. 1995, *ApJ* 447, 82
- Rodgers A.W. 1977, *ApJ* 212, 117
- Ruphy S., Robin A.C., Epchtein N. et al. 1996, *A&A* 313, 21
- Sackett P.D. 1997, preprint astro-ph/9608164, accepted by *ApJ*
- Sadler E.M., Rich R.M., Terndrup D.M. 1996, *AJ* 112, 171
- Sellwood J.A. 1985, *MNRAS* 217, 127
- Sellwood J.A. 1993. In: Holt S.S., Verter F. (eds) Back to the Galaxy. New York, AIP, p. 133
- Sellwood J.A., Sanders R.H. 1988, *MNRAS* 233, 611
- Sharples R., Walker A., Cropper M. 1990, *MNRAS* 246, 54
- Sommer-Larsen J., Flynn C., Christensen P.R. 1994, *MNRAS* 271, 94
- Spaenhauer A., Jones B.F., Whitford A.E. 1992, *AJ* 103, 297
- Spergel D.N., Malhotra S., Blitz L. 1997, in preparation
- Stanek K.Z., Udalski A., Szymanski M. et al. 1997, *ApJ* 477, 163
- te Lintel Hekkert P., Caswell J.L., Habing H.J., Haynes R.F., Norris R.P. 1991, *A&AS* 90, 327
- Tyson N.D., Rich R.M. 1991, *ApJ* 367, 547
- Udalski A., Szymanski M., Stanek K.Z. et al. 1994, *Acta Astron.* 44, 165
- Vallée J.P. 1995, *ApJ* 454, 119
- Verdes-Montenegro L., Bosma A., Athanassoula E. 1995, *A&A* 300, 65
- Wada K., Taniguchi Y., Habe A., Hasegawa T. 1994, *ApJ* 437, L123
- Wamsteker W. 1981, *A&A* 97, 329
- Weiland J.L., Arendt R.G., Berriman G.B. et al. 1994, *ApJ* 425, L81
- Weiner B.J., Sellwood J.A. 1996. In: Blitz L., Teuben P. (eds.) Proc. IAU Symp. 169, Unsolved problems of the Milky Way. Dordrecht, Kluwer, p. 145
- Wielen R. 1977, *A&A* 60, 263
- Worthey G. 1994, *ApJS* 95, 107
- Zhang X. 1996, *ApJ* 457, 125
- Zhao H.S. 1996, *MNRAS* 283, 149
- Zhao H.S., Mao S. 1996, *MNRAS* 283, 1197
- Zhao H.S., Rich R.M., Spergel N.D. 1996, *MNRAS* 282, 175
- Zinn R. 1985, *ApJ* 293, 424

This figure "fig4.gif" is available in "gif" format from:

<http://arxiv.org/ps/astro-ph/9706242v1>

This figure "fig10.gif" is available in "gif" format from:

<http://arxiv.org/ps/astro-ph/9706242v1>

This figure "fig10bis.gif" is available in "gif" format from:

<http://arxiv.org/ps/astro-ph/9706242v1>